Multi-modal refinement of the human heart atlas during the first gestational trimester

Authors

Christopher De Bono[1], Yichi Xu[2,*], Samina Kausar[1,*,£], Marine Herbane[1], Camille Humbert[1], Sevda Rafatov[1], Chantal Missirian[1,3], Mathias Moreno[1], Weiyang Shi[4], Yorick Gitton[5], Alberto Lombardini[6], Ivo Vanzetta[6], Séverine Mazaud-Guittot[7], Alain Chédotal[5], Anaïs Baudot[1], Stéphane Zaffran[1,✪] and Heather C. Etchevers[1,✪]

Affiliations

[1] Aix Marseille Univ, INSERM, MMG (Marseille Medical Genetics), Marseille, France

[2] Department of Systems Biology for Medicine and Frontier Innovation Center, School of Basic Medical Sciences, Fudan University, Shanghai 200032, China

[3] Medical Genetics Department, Assistance Publique Hôpitaux de Marseille, La Timone Children's Hospital, Marseille, France

[4] Department of Laboratory Medicine, Renji Hospital, School of Medicine, Shanghai Jiao Tong University, Shanghai, China

[5] INSERM, CNRS, Institut de la Vision, Sorbonne Université, Paris, France

[6] Aix Marseille Univ, CNRS UMR 7289, INT (Institut de Neurosciences de la Timone), Marseille, France

[7] Inserm, EHESP, Irset (Institut de recherche en santé, environnement et travail), UMR_S1085, Université Rennes, Rennes, France

* These authors contributed equally to this work.

✪ Co-last and corresponding authors.

[£] Current address, Wellcome – MRC Cambridge Stem Cell Institute, Jeffrey Cheah Biomedical Centre, University of Cambridge, Cambridge, CB2 0AW, UK.

1. Abstract

Forty first-trimester human hearts were studied to lay groundwork for further studies of principles underlying congenital heart defects. We first sampled 49,227 cardiac nuclei from three fetuses at 8.6, 9.0, and 10.7 post-conceptional weeks (pcw) for single-nucleus RNA sequencing, enabling distinction of six classes comprising 21 cell types. Improved resolution led to identification of novel cardiomyocytes and minority autonomic and lymphatic endothelial transcriptomes, among others. After integration with 5-7 pcw heart single-cell RNAseq, we identified a human cardiomyofibroblast progenitor preceding diversification of cardiomyocyte and stromal lineages. Analysis of six Visium sections from two additional hearts was aided by deconvolution, and key spatial markers validated on sectioned and whole hearts in two- and three-dimensional space and over time. Altogether, anatomical-positional features including innervation, conduction and subdomains of the atrioventricular septum translate latent molecular identity into specialized cardiac functions. This atlas adds unprecedented spatial and temporal resolution to the characterization of human-specific aspects of early heart formation.

Introduction

The heart is the first permanent organ to perform a vital function in all vertebrate embryos and many invertebrates (Maldonado et al., 2019). Its anatomy and output, however, vary widely across species. Understanding the normal development of human heart cells and tissues is essential for improving the diagnosis, treatment and prognosis of congenital heart defects (CHDs), the most common malformations at birth.

Due to difficulties studying human tissue directly, much of our knowledge about molecular, cellular, and morphogenetic processes driving heart development comes from animal models. While severe CHDs are often established by the sixth week of gestation, leading to spontaneous abortion, other serious or fatal defects emerge in heart regions influenced by human-specific factors like shear stress, growth, and anatomical changes that modulate cardiac function through birth (Oparil et al., 1984). These factors are difficult to reproduce in popular vertebrate models.

The late embryonic and early fetal period, at the end of the first trimester, marks a critical developmental phase of cardiac remodeling, but due to limited tissue availability it is challenging to study in humans (Hikspoors et al., 2022; O'Rahilly, 1971). Integration of new findings from additional samples is necessary for a representative atlas of prenatal cardiac cell types, functions, anatomical positions and interactions across human cellular and individual diversity (Asp et al., 2019; Cao et al., 2020; Farah et al., 2024; Hou et al., 2024; Lázár et al., 2024; Leshem et al., 2024; Xu et al., 2023).

Such integration is not trivial. Fetal heart cells produce hundreds to thousands of stage-specific transcripts and paralogous genes to those defining cell types in other parts of the body or at later life stages (D'Antonio et al., 2022). Tiny percentages of cells contact fluids or populate valves, ganglia and coordinate rhythmic contraction, requiring deep, unbiased sampling to be comprehensive. Mammalian fetal hearts display physiological properties mediated by connective tissues from various developmental lineages, about which little is known in humans (Ali et al., 2014; Deng et al., 2023; Dettman et al., 1998; Dewing et al., 2022; Gittenberger-de Groot et al., 1998; Norris et al., 2009; Vrancken Peeters et al., 1999). These considerations complicate efforts to assign cell identities on the basis of prior knowledge.

To address these challenges, we analyzed human hearts between 8 to 11 post-conceptional weeks (pcw), bridging embryonic and fetal stages. We generated *de novo* molecular and anatomically informed datasets about their composition using spatial and single-nucleus transcriptomics. Integrating published atlases, we also identified and validated novel markers, intermediates in lineage diversification, and features of the atrioventricular septation complex.

This refined atlas enhances understanding of cellular differentiation, function and spatial organization in the developing human heart.

52 **Results**

53 Increasing the resolution of biologically meaningful human 54 cardiac cell types

55 To characterize even rare cells, we analyzed a total of 40 human embryonic and fetal hearts
56 of 6.5-12.3 post-conceptional weeks (pcw) with careful anatomy, histology (Supplementary
57 Figure S1) and complementary transcriptomics approaches, followed by spatial validation of
58 transcript and protein expression in sliced and/or intact organs.

59 Cell type assignment at single-nucleus resolution

60 To preserve cellular diversity among heterogeneous populations, we used single-nucleus
61 RNA-sequencing (snRNAseq). Nuclei were isolated from whole hearts with proximal great
62 vessels from one female (8.6 pcw) and two male (9.0 pcw and 10.7 pcw) fetuses
63 (Supplementary Materials and Methods; Fig. 1A). We analyzed snRNAseq transcriptomes for
64 18,129, 8,750, and 22,348 individual nuclei respectively, and integrated the 49,227 fetal
65 cardiac nuclei to assign group identities. Six classes comprising 21 clusters were distinguished
66 (Fig. 1B) and their identities assigned using known markers and a post-hoc literature search
67 for co-expressed, differentially expressed genes (DEGs) when comparing a cluster against all
68 others (Table S1). All clusters were found in varying numbers in a hearts, such as fewer arterial
69 smooth muscle cells (SMC) at 10.7 pcw (Fig. 1C-D). This specimen had relatively truncated
70 distal segments of the outflow tract (Fig. S1).

71 Markers such as *MYH6* and *MYH7* (Lu et al., 2022) for cardiomyocytes (I), *POSTN* and
72 *PECAM1* for cardiovascular endothelial cells (II), and *EBF2 and PRRX1* for interstitial
73 fibroblasts and smooth muscle for stroma (III), allowed grouping of functionally related clusters
74 into classes. Epicardial (IV), blood and immune cell (V) and neural crest-derived (VI) cells
75 were also designated classes (Fig. 1D-F).

76 Iterative refinement of annotations

77 Class I cardiomyocytes (29,233 nuclei, 59.4% of total; Table S1, tab 2) broadly expressed
78 *MYH6* and *MYH7* (Fig. 1E-G). Their relative abundance distinguished subclasses of atrial
79 (CmA1-A4; *MYH6*^{hi}) and ventricular chambers (CmV1, CmV2, CmVCnD; *MYH7*^{hi}),
80 respectively, reflecting histological (Fig. S1) and functional differences. Significant DEGs from
81 each class and within- or between-class DEGs, are available in Table S1.

82 The CmG2M cluster (8.3% of class) had higher representation of G2M transition
83 characteristics, including significant DEGs encoding the centriolar assembly proteins *CENPF*
84 and *CENPP*; *ANLN* (cytokinesis); *KIF18B* and *KIF15* (kinesin superfamily); and *BRIP1*, a
85 BRCA1-interacting helicase. CmMit represented mitotic cardiomyocytes (3%). Its significant
86 DEGs encoded *MKI67*, centriolar *CENPE*, the cell cycle kinase *AURKA*, and the mitosis-
87 initiating *CCNB1*. *MYH7* and *TTN* were among DEGs of the ventricular cluster CmV1 (32.2%,
88 Fig. 1G) but CmV1 also uniquely co-transcribed *KCNQ5* (potassium channel Kv7.5) and
89 *INPP4B* (a PI3K signaling suppressor; Fig. S2A). This combination may underscore the
90 specific electrical properties of ventricular cardiomyocytes.

91 CmA2 and CmV2 spanned atrial and ventricular subclasses (4.4 and 3.4% of Class I cells;
92 Fig. 1D, Table S1). With *PAM*, *TBX5* and *MYH6* as DEGs, CmA2 also expressed the highest
93 atrial levels of *CACNA1D* (Table S1, tab 7). *CACNA1D* encodes the L-type voltage-activated
94 calcium channel CaV1.3 of the sinoatrial node (van Eif et al., 2019). CmV2, like CmVCnD,
95 expressed *KCNIP4* (a voltage-gated potassium channel interacting protein) but like CmA2,
96 expressed the AV bundle adhesion contactin *CNTN5* (Fig. 1G) (Kanemaru et al., 2023;
97 Smirnov et al., 2018). CmVCnD differed from CmV2 and other ventricular cardiomyocytes
98 (Table S1, tab 6) by *NAV3* (neuron navigator 3), an axon guidance cue required for zebrafish
99 heart morphogenesis (Lv et al., 2022). Other CmVCnD markers included *NLGN1*, encoding a
100 ligand for post-synaptic neurexins of neuromuscular junctions (Ramesh et al., 2021) and
101 *SORCS3*, a neurotrophin uptake receptor necessary for post-synaptic vesicular trafficking
102 (Oetjen et al., 2014) (Fig. 1G). CmA2, CmV2 and CmVCnd distinguished cell states and/or
103 locations of the developing human pacemaker (sinoatrial and atrioventricular nodes) and
104 conduction system.

105 Rare clusters were assigned identities by comparing DEGs first to all other heart nuclei, then
106 to the other clusters within their class, and leveraging Enrichr-KG (Evangelista et al., 2023) for
107 significantly enriched annotations from the Descartes human fetal atlas (Cao et al., 2020), the
108 Human Gene Atlas (Su et al., 2004), the Tabula Sapiens (The Tabula Sapiens Consortium,
109 2022), the KEGG 2021 Human, and the Gene Ontology Biological Process databases (Fig.
110 S2B). For example, neural crest-derived Class VI (*NRXN1*, *CDH6*) subdivided into
111 neuroendocrine (NE; 227 nuclei; Fig. 1E-G, Fig. S2B) and Schwann cell precursor (SCP; 309
112 nuclei; Fig. 1G, Fig. S2C) clusters. *NRG1*, *GATA3* and *ALK* (Boeva et al., 2017) distinguished
113 NE from SCP (*EDNRB*, *CDH19*) (George et al., 2018).

114 The smallest EnVL (venous-lymphatic endothelium) Class II cluster of 210 cells (Fig. 1B, G)
115 co-expressed established markers like *FLT4* (*VEGFR3*) and *TBX1* (Fig. 1G; Table S1) (Wang
116 et al., 2023). Although intentionally rinsed away during collection, blood-derived Class V (655
117 nuclei) included fetal hemoglobin-expressing (*HBG1*/*HBG2*) erythrocytes, *RUNX1*-expressing

immature and *PTPRC* (CD45)-expressing differentiated hematopoietic progeny, and *SPP1*-positive macrophages (Fig. 1D-E).

Integration of first-trimester cardiac atlases at cellular resolution identifies an early cardiomyofibroblast progenitor

We integrated our snRNAseq data with two human heart atlases derived from single-cell (sc)RNAseq of whole human embryos aged 4-6 pcw (8,266 cells) (Xu et al., 2023) and a 6.5-7 pcw heart (3,717 cells) (Asp et al., 2019) to analyze transcriptomic changes over time (Fig. 2A). Similar integration of scRNAseq and snRNAseq datasets has enabled identification of minority progenitors in mouse skeletal muscle (McKellar et al., 2021).

Cardiomyocytes and stromal cells in the mouse derive from common mesodermal progenitors that begin lineage restriction as early as gastrulation (Lescroart et al., 2014). To search for evidence of similar human fate engagement, we integrated cells assigned to stromal or cardiomyocyte classes (I and III, Fig. 1D) between 5 pcw (Carnegie Stage [CS]13) and 10.7 pcw. We then performed dimensional reduction with Potential of Heat-diffusion for Affinity-based Trajectory Embedding (PHATE), a diffusion-based manifold learning method (Moon et al., 2019) (Fig. 2A-C; Fig. S3C-D). The new clusters corresponded on a one-to-one or one-to-many basis with our snRNAseq cell type assignments (Fig. S3A-B). Some assignments were nearly exclusive to later cells, including clusters 8 (CmA3) and 2 (CmA4) as well as a stromal progenitor in cluster 15 (Fb3) (Fig. 2D-F). In contrast, cells from the 6.5-7 pcw heart (Asp et al., 2019) were relatively impoverished in cardiomyocytes and their precursors (Fig. 2F), perhaps due to technical loss of larger cells *versus* size-agnostic nuclei.

Not all clusters were equally populated by stage; one in particular appeared more represented at CS15-16 (6 pcw) than at later stages (Fig. 2A-C, box). Slingshot trajectory analysis (Street et al., 2018) superimposed on this new projection traced classes I and III back to a common cardiomyofibroblast (cluster 16, CmF), mostly depleted after 6 pcw (Fig. 2D). A confusion matrix between the full scRNAseq/snRNAseq dataset (Fig. 2E) and our original clusters (Fig. 1) showed little overlap between CmF and later clusters belong to cardiomyocyte or stromal classes, although some CmF persisted even at 10.7 pcw (Fig. 2C, F).

CmMit (cluster 6) and Fb3 (cluster 15) were the nearest class-specific progenitors to CmF (Fig. 2D). To identify which more resembled parental CmF, we classified all significant DEGs into “high” or “low” bins, scoring how these categories were inherited over the trajectory from cluster 16 to 6 or to 15 during differentiation. Most CmF genes (Table S2) were maintained

150 from CmF to CmMit but newly transcribed in Fb3, suggesting closer lineage ties to proliferating
151 cardiomyocyte progenitors (Fig. 2G).

152 In summary, our snRNAseq data segregated into six classes and 21 cell clusters, highlighting
153 relevant cardiomyocyte identities, rare cell types, anatomical and developmental features.
154 Integrating existing data, we identified new progenitor states and modeled lineage
155 relationships. These findings enhance current understanding of human cardiac cell
156 diversification and organization.

157 Spatial transcriptomics of multiple 8.4 and 9.7 pcw heart sections

158 To add positional context, we undertook 10x Genomics Visium spatial transcriptomics (ST)
159 analysis on two sections from an 8.4 pcw male heart and four sections from a 9.7 pcw female
160 heart (Fig. 1A), assessing over 12,000 regularly spaced tissue spots (Supplementary
161 Materials and Methods). We identified eight clusters in 8.4 pcw sections and 6-8 at 9.7 pcw
162 (Figs. S4-9). Cluster information was then projected onto each section at appropriate
163 coordinates. Histological landmarks (Fig. S1) and known markers permitted us to assign
164 cluster identities: for example, compact or trabecular *MYH7*+ ventricular cardiomyocytes
165 (*HEY2 and IRX3*, respectively). *MYH6*+ atrial cardiomyocytes expressed *BMP10* and *TBX5*
166 on the right and *PITX2* on the left. Arterial smooth muscle enriched in *ELN* and *MYH11* was
167 identified at both stages, as were discrete clusters of valvular (*SCX*, *PENK*) or subvalvular
168 (*POSTN, PRRX1*) stroma. Full lists of markers in individual section clusters are provided
169 (Table S3). Integration of these datasets distinguished 14 clusters (abbreviated SIC to
170 distinguish from snRNAseq clusters), improving cell type comparisons across time and space
171 (Fig. 3A, B, and Fig. S10; Table S4). Left and right, compact and trabecular cardiomyocyte
172 clusters expressed expected genes (Fig. 3B, C), but integration enabled better discrimination
173 of non-contractile cell types with spatial coherence (Table S4).

174 The ascending aortic SMC (SIC12; *ELN*+) was clearly distinct at both stages from thick-walled,
175 extracardiac arteries. *Tunica adventitia* (SIC7; *COL1A1*+) of the ascending aorta and coronary
176 arteries was further abluminal. SIC6 included both myofibroblasts (*PRRX1*, *DCN, FN1,*
177 *COL1A2, COL3A1*) and encased autonomic neurons (*NEFL*, *TUBB3*, *PRPH*, *PHOX2B*). The
178 valves (SIC10) expressed *SCX* (Fig. 3C) and *POSTN*, but SIC5 and SIC12 were also strongly
179 enriched in *POSTN*. Epicardial identity (SIC9) was marked by *TBX18* and *ITLN1* (Sacks and
180 Fain, 2007). The cardiac conduction system, with the fewest spots, corresponds in these
181 sections to the sinoatrial node (SIC13; *SHOX2*, *TBX3*), demonstrating improved cell type
182 annotation by adding ST (Table S4; Fig. 3A-C).

183 Immunofluorescence validated MYL7, MYH6 and MYH7 protein distribution (Fig. 4). Myosin
184 is a hexamer composed of four light and two heavy chains, necessary for contractility. Myosin
185 regulatory light chain 7 (encoded by *MYL7*) is a human atrial-specific gene, expressed from 8
186 pcw until after birth (Hailstones et al., 1992). While *MYL7* was initially pan-cardiac (8.4 pcw,
187 Fig. 4A-B), it was predominantly atrial by 9.7 pcw (Fig. 4C), consistent with its
188 immunoreactivity at 9.0 pcw (Fig. 4D) and confirming *in situ* hybridization at the same stage
189 (Hailstones et al., 1992). MYH6 and MYH7 were detected in the atria and the ventricles at 9.0
190 and 12.0 pcw respectively (Fig. 4E-L). As predicted from avian data (Teichmann and Kessel,
191 2004), *BMP10* was enriched in ventricular trabeculae and the right atrium (Fig. 4M), as
192 confirmed by RNAscope at 9.0 pcw (Fig. 4N-P).

193 Integrated spatial transcriptomics refined our fetal heart atlas by adding positional context,
194 enabling finer identification of certain cell types and expression dynamics over time.

195 Deconvolution of spot transcriptomes

196 Each spot in sequencing-based ST may contain distinct cell types in varying proportions. To
197 measure this heterogeneity, we deconvoluted each spot using the Robust Cell Type
198 Decomposition (RCTD) method (Cable et al., 2022), referencing our integrated snRNAseq
199 data. Relative cell-type proportions were projected back onto the six heart sections, turning
200 each spot into pie charts of relative snRNAseq cluster proportions (Fig. 5, Fig. S11-16).

201 Figure 5 highlights 8.4 pcw heart section A91 and 9.7 pcw heart section A17. Pie charts depict
202 snRNAseq cell types per spot (Fig. 5 A,C). Deconvolution results were further averaged in
203 each of the 14 ST clusters across the 6 integrated ST datasets (Fig. 5 A,C; Table S5) as large
204 pie charts with mean snRNAseq cell type proportions in SIC0 (right ventricular compact
205 myocardium), SIC2 (trabeculae), SIC3 (right atrial cardiomyocytes), SIC4 (left atrial
206 cardiomyocytes), SIC7 (*tunica adventitia*), SIC10 (valves), SIC12 (aorta, vascular SMC) and
207 SIC13 (conduction system). For example, at 8.4 pcw (Fig. 5A), SIC0 comprised on average
208 40% CmVCnD, 15% CmV1, 19% CmG2M and 12% EnTh profiles among others, while SIC10
209 contained on average 73% FbVIC cells, 6% EndoCd and 7% of EnTh cells.

210 Deconvolution results for sections A91 (8.4 pcw) and A17 (9.7 pcw) are shown in Fig. 5B D,
211 with estimated relative proportions of the following clusters from integrated snRNAseq data:
212 CmVCnD, CmV1, CmG2M, CmA1, CmA2, CmA3, CmA4, CmMit, EnTh, EndoCd, Fb1, Fb2,
213 FbVIC, SMC and EpiCd. Similar proportions were observed across all sections (Figs. S11-16;
214 Table S5).

Discrete chamber identities by the third gestational month

Deconvolution refined integrated snRNAseq cluster identities. For example, at 8.4 pcw (A91), right atrium spots (SIC3) averaged 30% CmA4 and 12% CmA1, while left atrium spots (SIC4) averaged 40% CmA3 but also 5% CmV1, 6% CmG2M and 3.5% CmA1 (Table S5). CmA4 correlated to right atrial identity and CmA3 with left, but their purported progenitor CmA1 (Fig. 2D) appeared in both atria (Fig. 5B, D).

The CmA2 cluster mapped to sinoatrial and atrioventricular nodes, which for the former was observed across multiple sections at each stage (Fig. 5B, arrows; Figs. S11-16). CmVCnD cluster dominated in the right ventricle, while CmV1 was more prominent in the left ventricle; these identities were observed in compact and trabecular myocardium (Fig. 5B, D). CmV2 mapped to trabeculae and a septal subvalvular domain, while EndoCd designated trabecular endocardium. SMC of aorta and extracardiac arteries surrounded EnTh while Fb1 localized to the *tunica adventitia*, capping the ventricles under the atria (Fig. 5 and Figs. S11-16).

Combining snRNAseq and ST data revealed extensive cell-type heterogeneity and refined identities of snRNAseq clusters. We appended positional terms (*eg*. left/right atria, subvalvular, atrioventricular node) to snRNAseq cluster names (Fig. 5) and confirmed distinct identities of endocardium and vascular endothelia.

Multi-omics identifies small cell clusters and rare transcripts

Integrating the two modalities allowed us to highlight cell markers not previously implicated in human cardiac development. Fibroblast and mural cell types in the mouse are functionally diverse and site-specific (Muhl et al., 2020). To identify similar specializations, we compared the combined list of genes significantly enriched in the clusters of snRNAseq stromal Class III (Table S1) with those significantly enriched in six spatial clusters corresponding to valves, subvalvular and connective tissue, *tunica adventitia*, extracardiac vessels and aortic SMC (Table S4). *PENK*, enriched in FbVIC in snRNAseq analysis, was expressed both in and between valves in ST (Fig. 6A, Fig. S17). Other valve DEGs included *BOC*, *INHBA*, *LTBP2*, *MEOX1*, *PTN*, *PTPRZ1*, *PRRX1*, *ROBO1,* and *RSPO3* (Fig. 6A, Fig. S17).

RNAscope analysis in additional specimens confirmed *PENK* distribution (Fig. 6D, F, F', M, N). *ACTA1* (Actin Alpha 1, Skeletal Muscle), was the top DEG of the complementary subvalvular ST cluster (Table S4; Fig. 7). RNAscope validated *ACTA1* expression at the ventricular attachment points of the valvular leaflets and the chordae tendineae (the "heart strings"; Fig. 6E, F, F'). ST analysis predicted mutually exclusive domains for *ACTA1* and *PENK* (Fig. 6G), which we confirmed by RNAscope (Fig. 6G'). Comparison of subvalvular ST

248 DEG to other stromal class clusters (6, 7, 10, 11, 12) found common differential expression of
249 only two genes, both cell cycle-associated: *ANLN* and *CDK1* (Table S4). Consistently,
250 CmG2M contributed most to the subvalvular domain, at over 19%, but CmV2, CmVCnd and
251 CmV1 were close behind (Table S5).

252 Mesenchymal homeobox-1, *MEOX1*, which regulates fibrosis of injured postnatal hearts
253 (Alexanian et al., 2021), was significantly enriched in FbVIC and Fb1 fibroblasts as shown by
254 snRNAseq (Table S1) and transcribed in atrioventricular (AV) valves (Fig. 6G, K, M') . *PRRX1*,
255 a widely expressed master transcription factor associated with conduction anomalies and a
256 top DEG characteristic of CmVCnd (Guo et al., 2021; Ke et al., 2022; Lee et al., 2022), was
257 co-expressed with *MEOX1* in the tricuspid valve (Fig. 6I, M, M'). We confirmed that *PRRX1*
258 was transcribed not only in AV and aortic valves, but also in the subvalvular domain (SIC5)
259 and ventricular trabeculae (SIC2; Fig. 6H, J, L).

260 The connective tissue cluster SIC6 featured co-expression of many genes associated with
261 autonomic nerve development, including *ISL1*, *TH*, *PRPH*, *PHOX2A*, *PHOX2B*, *PRRX1*,
262 *DLK1*, *PENK*, *TBX2, GAP43*, *L1CAM*, *STMN2* and *TUBB3* (Fig. S18). RNAscope and
263 immunofluorescence analysis confirmed complementary expression of PRPH protein and
264 *ISL1* and *PRRX1* transcripts (Fig. 7A-C). SIC6 thus also comprises embedded cardiac ganglia.
265 Overall, these results validated the different modes of transcriptional analysis, including
266 deconvolution of ST spot heterogeneity with a snRNAseq reference.

267 Toward a four-dimensional atlas

268 Cell types along reticulated blood vessels, connective tissues and nerves are represented in
269 all organs, but can be difficult to detect in ST because of low absolute cell numbers or fine
270 layers with distinct functions. The 536 (1.1% of total) cells assigned to neural crest-derived
271 Class VI were not well resolved by ST outside a ganglion fortuitously sampled in section A90.
272 The 7,224 transcriptomes of endocardial, vascular or lymphatic endothelial cells were not as
273 well mapped as abluminal SMC and connective tissue. Although we had identified clusters
274 corresponding to neuronal (*PRPH*+) and endothelial (*PECAM1*+) cells (Fig. 1 and Fig. 8A, D),
275 the logic of their anatomic distributions was invisible in ST (Fig. 8B, E). Two physical
276 dimensions are insufficient to represent the architecture of blood vessels and peripheral
277 nerves within and surrounding the heart (Fig. 8C, F).

278 Whole-organ immunofluorescence after tissue clearing has enabled better sampling of
279 peripheral nerve ramifications and lacrimal gland development over time (Belle et al., 2017;
280 Blain et al., 2023). We used whole-organ immunofluorescence to examine spatial
281 arrangements of blood vessels and peripheral nerves in ten fetal human hearts (Fig. 8G-L and

282 Supplementary Movies 1-4), as well as markers of other cell types (*eg*. ALDH1A1, FABP4,
283 MYH6, POSTN; Fig. S19). Light-sheet confocal microscopy resolved expression of these
284 proteins at a cell-to-tissue scale, to bridge annotations of cell types and their true spatial
285 distributions.

286 The great arteries of the outflow tract were more densely innervated than the cardiac apex,
287 and innervation progressed in a proximal-to-distal manner over time between 7 and 10 pcw
288 (Fig. 8G, J; Fig. S19F-H). Nerves tracked with blood vessels on the outside of the heart before
289 penetrating the muscle more robustly in the ventricles than the atria (Fig. 8G, J). The
290 endocardial lining of all valvular cusps and atria, like the arterial trunk and coronary veins,
291 showed sparse PECAM1 immunofluorescence compared to the strong signal of coronary
292 arteries (Fig. S19).

293 The valves themselves were devoid of nerves at all stages examined (Fig. 8I, L; Fig. S19F).
294 DEGs of FbVIC, NE and EndoCd (Table S1) respectively encoded candidate repulsion
295 mediators annotated by Gene Ontology as mediating negative chemotaxis (GO:0050919)
296 such as *ROBO1*, *SEMA6A*, *SEMA3D* and *PLXNA4* (FbVIC); *SLIT3*, *SEMA3C*, *SEMA6D*,
297 *UNC5B, UNC5*C, *UNC5D*, *DCC* and *DSCAM* in cardiac neurons; and *NTN1*, *PLXNA4* and
298 *PLXND1* in the endocardium. We used CellChat (Jin et al., 2024) to identify the most likely
299 pairs of transcripts encoding ligands from the valves and receptors on axons or their SCP.
300 CellChat predicted that the most significantly probable interaction would be engagement of
301 PTPRZ1 receptors on nerve Schwann cells by inhibitory ligands MDK and PTN (Fukada et al.,
302 2006), produced by endothelial cells and FbVIC (Fig. S17, Fig. S20A). Network analysis
303 associates these three interactants with "positive regulation of glial differentiation
304 (GO:456787)" (Fig. S20B-C), implying that perivalvular nerves may stabilize rather than sprout
305 into leaflets. Nerves themselves could be prevented from pathfinding there by FbVIC-secreted
306 PTPRS or EnTh-produced SEMA3D (Fig. S20A), also likely candidates.

307 Discussion

308 In this work, we independently analyzed whole fetal human hearts using single-cell and spatial
309 transcriptomics, and enriched cell-type annotations with spatial and anatomical information
310 from additional samples, to obtain a comprehensive overview into a vulnerable window of
311 human cardiac development. We highlight an approach also taken by others (Farah et al.,
312 2024; Knight-Schrijver et al., 2022) to conduct iterative refinements based on fully accessible
313 data to update "ground truth" in all developing organ atlases. While new contributions, whether
314 replicative or novel, could seem incremental, they play a critical role in addressing gaps in
315 current knowledge by increasing statistical power. Building a comprehensive, community-

driven developmental human cell atlas requires an open, iterative process where scientists can continuously reinterpret and enhance their discoveries in light of new findings and technical approaches (Haniffa et al., 2021).

Identification of previously undescribed cell types and states

We distinguished nine populations of cardiomyocytes after analyzing 49,227 nuclear transcriptomes from human hearts at 8.6, 9.0, and 10.7 pcw. Among these, two were in a state of preparing for or undergoing active proliferation (CmG2M and CmMit). These comprised 14% and 3% of total cardiomyocytes, respectively, and are at least ten times scarcer in postnatal human hearts (Bergmann et al., 2009). In mice, most cardiomyocytes undergo a final round of nuclear mitosis and cell division near birth, producing post-mitotic, multinucleated or polyploid cells needed to build a sarcomeric scaffold for a lifetime of contraction (Soonpaa et al., 1996). Similarly, most postnatal human heart cells are post-mitotic. This atlas provides a critical reference to normal human development for improving maturation of induced pluripotent stem cells for cell therapy in such conditions as hypoplastic left heart syndrome (Krane et al., 2021) or infarction (Jiang et al., 2024) or to study principles of human cardiac self-organization (Kostina et al., 2024; Lewis-Israeli et al., 2021).

Integration with earlier available datasets revealed a trajectory diversifying novel fibroblast types such as FbVIC from a common progenitor to stromal and cardiomyocyte lineages. Genetic lineage tracing in stem cell-derived organoid or gastruloid models could clarify the potential, contributions and responses of such cardiomyofibroblast progenitors (Argiro et al., 2024; Kostina et al., 2024). Further dataset integration when made available (Bayraktar et al., 2024; Cranley et al., 2024; Lázár et al., 2024) may resolve more of the nature, contributions and competence of stromal cell types in the fetal heart and beyond.

Stromal diversity reflects anatomical specializations

Fibroblasts are extracellular matrix and growth factor-secreting cells of remarkable functional, organizational and lineage diversity. Epicardial cells predominantly contribute to intracardiac fibroblasts in mice (Ali et al., 2014). However, endocardial and endothelial cells also contribute, particularly in the ventricular septum and chamber walls (Deng et al., 2023; Liu et al., 2018). Furthermore, neural crest cells can differentiate into migrating pericytes, fibroblasts, SMC and even melanocytes in the proximal great vessels, valves, and the septal atrioventricular junction (Etchevers et al., 2001; Hulin et al., 2019; Jiang et al., 2000; Le Lièvre and Le Douarin, 1975). Although no melanocytes were identified in these first-trimester human hearts, *CHD6*

348 (cadherin-6) emerged as a marker of neural crest-derived Class VI cells, with some persistent
349 mesenchymal features at the stages assessed (Clay and Halloran, 2014).

350 According to the specific valve and even leaflet, valvular interstitial cells (FbVIC) have distinct
351 developmental origins but convergent functions. In atrioventricular (inlet) valves, FbVIC arise
352 mostly from endocardial and epicardial cells, while arterial (outflow) valves include
353 contributions from neural crest, endocardial, and second heart field cells (El Robrini et al.,
354 2016; Etchevers et al., 2001; Jiang et al., 2000; Le Lièvre and Le Douarin, 1975; Liu et al.,
355 2018; Liu et al., 2023; Waldo et al., 1998). FbVIC and SMC are spatially restricted, but Fb1 is
356 also, with more cells in the *tunica adventitia* and proximal ventricles. Our findings confirm that
357 many human cardiac fibroblasts derive from non-epicardial progenitors, as in mice (Deng et
358 al., 2023). Trajectory analysis over integrated 5-10 pcw data shows that epicardial cells had
359 already segregated from the common cardiomyofibroblast (CmF) lineage branch in
360 cardiogenic mesoderm. By 8.6 pcw, CmF had diverged into dividing progenitors contributing
361 preferentially to either stromal or cardiomyocyte lineages. CmF-derived stroma likely
362 contributes via Fb3 fibroblasts to diverse mesenchymal cell types, with FbVIC segregating
363 earlier than other fibroblasts or SMC.

364 Complementary information from ST adds atlas precision

365 Spot clusters, dominated by cells with similar transcriptional profiles, link cardiac cell
366 localization and function when mapped back to anatomically and functionally distinct regions.
367 For instance, *BMP10* was expressed in ventricular trabeculae, as shown in chicken and mouse
368 (Chen et al., 2004; Teichmann and Kessel, 2004), but also in the right atrium, consistent with
369 its asymmetric enrichment in pectinate muscles of mice and humans (Ho et al., 2002; Sedmera
370 et al., 2000). While BMP10's role remains unclear, thickened pectinate muscle junctions with
371 the lateral right atrial wall of diseased adult human hearts *ex vivo* correlate with persistent
372 atrial fibrillation (Zhao et al., 2023).

373 This atlas shows that *BMP10* co-varies spatially in the right atrium and in specific
374 cardiomyocytes (CmA1/CmA4 populations; Table S1) with the *PRKAG2* gene (Fig. S21).
375 *PRKAG2* loss-of-function is responsible for congenital, progressive cardiomyopathies with
376 high rates of life-threatening atrial fibrillation and/or ventricular hypertrophy, glycogenosis or
377 tachycardia (Blair et al., 2001; Gollob et al., 2001; White-Brown et al., 2024). A human
378 microdeletion syndrome affecting BMP dosage phenocopies *PRKAG2* hypomorph alleles
379 (Lalani et al., 2009). Our observation provides further evidence that BMP receptor-mediated
380 signal transduction is needed to establish the *annulus fibrosis* at the atrioventricular junction

381 (Gaussin et al., 2005), preventing damaging electrical coupling outside of the pacemaker
382 circuit.

383 We observed left atrial *PITX2* expression in both transcriptomic modes. Early lateralization
384 reinforced by hemodynamics enhance molecular differences between left and right heart cells
385 in many embryonic models (Hill et al., 2019; Liu et al., 2002; Nowotschin et al., 2006). Laterality
386 establishment by *Pitx2* influences outflow tract morphogenesis and restricts pacemaker
387 development to the right atrium (Hill et al., 2019; Wang et al., 2010). PITX2 remains necessary
388 for adult cardiac adaptive responses (Kahr et al., 2011; Tao et al., 2016).

389 Integrating all ST data helped us assign spots to sparse structures like the sinoatrial node or
390 an autonomic ganglion. Spot deconvolution with the identities established by our single-
391 nuclear analyses improved prediction of the heterogeneous cellular composition of each spot,
392 and, in return, refined snRNAseq cluster annotation with spatial information. This was true for
393 neuroendocrine, endothelial *versus* endocardial, and trabecular cardiomyocyte identities.

394 We clarified the historical ambiguity about whether “endocardial” describes a positional or cell-
395 autonomous distinction from endothelial cells of arteries, veins, lymphatics and capillaries
396 (Wang et al., 1998); human fetal endocardium has both spatial and molecular specificities.
397 Furthermore, the multi-modal transcriptomic approach discriminated spatially restricted gene
398 expression within distinct cell types, such as *PENK*. *PENK* encodes proenkephalin, a
399 component of the neuroendocrine opioid system expressed in murine neural crest-derived
400 mesenchyme and valve primordia (Chen et al., 2022; Liu et al., 2019; Soldatov et al., 2019).
401 The *tunica adventitia*, encasing the proximal ventricles and outflow tract, was best
402 distinguished from other stroma in ST sections. We could more efficiently predict left *versus*
403 right ventricles, compact *versus* trabecular myocardium and conduction nodes *versus* likely
404 differentiating Purkinje cells in subpopulations of the snRNAseq datasets, finding specific and
405 sensitive markers to validate with these complementary techniques.

406 The combination of snRNAseq and ST provided complementary insights. The former offered
407 quantitative co-transcriptional information at single-nucleus resolution, while the latter
408 provided landmark associations such as chambers or valves, and coordinates relative to the
409 body plan (dorsal/ventral, anterior/posterior) and the organ itself (proximal/distal,
410 inside/outside). This integrative approach based on limited but well-chosen samples can be
411 applied to other organ atlases, adding informative dimensions by leveraging existing and new
412 data.

Sparse but widespread anatomical networks

The aforementioned methods may bypass rare and/or sparse cells in a sample, including nerves, lymphatics, specialized impulse-conducting cells, resident immune cells, vasculature and fascia. Synergy between next-generation sequencing- or image-driven transcriptomics, high-dimensional protein/mRNA labelling approaches, and qualitative and quantitative measurements enhances functional significance of cellular identity labels. Our 3D immunofluorescence image datasets for a selected time points and markers are a proof-of-concept that multiple networked biological structures can act as anatomical coordinates in the developing fetal and adult organs (Boppana et al., 2023). These datasets can support quantitative segmentation measurements over time and deep-learning model training (Kaltenecker et al., 2024).

Until this year, cell catalogues of the human heart had sampled relatively few individual cells during the critical late first-trimester period, overlooking important cell types and states. As performed for reasons of scale, sampling representative portions of larger organs (Litviňuková et al., 2020) or regressing out highly variable cell-cycle or ribosomal transcripts, as once performed in single-cell analysis pipelines (Butler et al., 2018), can exclude expected and functionally important minority populations. Autonomic neurons and glia, specialized attachment zones between tissues such as the *chordae tendineae*, endothelia, FbVIC and certain cardiomyocyte and mesenchymal progenitor states are among these. Our atlas iteration of the developing human heart situates these populations in their spatiotemporal and functional contexts, providing a reference and roadmap for future research.

Methods

Human embryo collection, staging and quality control

First trimester human embryos and fetuses (6-13 pcw) were obtained from induced terminations of pregnancy performed legally in France and sought for reasons other than known fetal abnormality. Tissues were collected after obtaining written consent from donors following procedural initiation, a protocol approved by the national Agency for Biomedical Research (authorization #PFS14-011 to SZ; Agence de la Biomédecine) and declared by the Human Developmental Cell Atlas (HuDeCA; https://hudeca.com) consortium to the French Ministry of Higher Education and Research under reference DC-2022-5011.

Sample collection

Terminations of pregnancy were induced using a standard combined mifepristone and misoprostol protocol, followed by aspiration. Gestational age was initially determined by ultrasound, refined by measurement of foot length (Evtouchenko et al., 1996; Hern, 1984; O'Rahilly and Müller, 1987; O'Rahilly and Müller, 2010), and confirmed through comparison and contribution of high-resolution photographs of our samples to a staged morphometric and histological cardiac atlas hosted at the Human Developmental Biology Resource (Gerrelli et al., 2015) (https://hdbratlas.org/organ-systems/cardiovascular-system/heart/dissections/gallery.html or https://bit.ly/HumanFetalHeart).

Intact hearts were recovered from aspiration detritus under a Zeiss binocular microscope, rinsed in ice-cold phosphate-buffered saline (PBS) and maintained on ice in Hank's buffered saline solution until further processing. Retained tissues were documented in a secure HuDeCA-wide database https://hudeca.genouest.org) using the OpenSpecimen biobanking LIMS (https://github.com/krishagni/openspecimen/; Krishagni Solutions, India).

Genotyping

Quantitative PCR was performed in duplicate on genomic DNA derived from lung or umbilical cord fragments using primers within *SRY* (ACAGTAAAGGCAACGTCCAG and ATCTGCGGGAAGCAAACTGC) to amplify a Y chromosome-specific fragment of 293 bp (Lardenois et al., 2023), and normalized to a 183 bp fragment of the *GAPDH* promoter on chromosome 12, amplified by CCACAGTCCAGTCCTGGGAACC and GAGCTACGTGCGCCCGTAAAA.

Genomic DNA from all samples were further annotated by molecularly determined sex and exclusion of large chromosomal-level copy number variations using a custom digital-droplet PCR analysis (StemGenomics iCS-Digital karyotypes (Assou et al., 2020)). Samples with ambiguous results were reanalyzed using subtelomeric Multiplex Ligation-dependent Probe Amplification (Aneuploidy MLPA probemix [P095], MRC Holland) or for sample HEF_DN_F0000467, with a diagnostic CGH array to exclude a smaller potential copy-number anomaly on chr22 with a high degree of confidence.

Single-nucleus RNA-sequencing

Three intact hearts from one female and two male fetuses (validated in the transcriptional data) were dissociated for single-nucleus incorporation into the GEMs of the 10X Chromium platform. Dissociation was begun by an initial crush in liquid nitrogen, continued with 10-20

476 strokes in a Dounce homogenizer over ice, and nuclei further separated from debris over a
477 discontinuous density gradient at 30-35% iodixanol as per a community protocol (Martelotto,
478 2021). Libraries were prepared by the Genomics and Bioinformatics facility (GBiM) of the
479 U1251 / Marseille Medical Genetics lab using the Chromium Next GEM Single Cell 3' Kit v3.1
480 (PN-1000269) with Dual Index Kit TT Set A (PN-1000215, 10X Genomics), according to
481 manufacturer's instructions.

482 Sequencing and raw data processing

483 All libraries were sequenced on a Nextseq 500 (Illumina) by the GBiM facility, except for
484 samples HEF_DN_F0000467 and HEF_DN_F0000530 on a Nextseq 500 by Integragen
485 (Evry, France). The sequenced snRNAseq libraries were processed and aligned to the human
486 reference genome (GRCh38-2020-A) using Cell Ranger software v.3.1.0 (10x Genomics),
487 with unique molecular identifiers (UMI) counted for each barcode.

488 Analysis, visualization and integration of snRNAseq datasets

489 Three datasets of snRNAseq from euploid hearts sequenced on different runs
490 (HEF_DN_F0000530, 8.6 pcw, female; HEF_DN_F0000374, 9.0 pcw, male;
491 HEF_DN_F0000467, 10.7 pcw, male) were analyzed using default parameters in the Seurat
492 4.1.1 pipeline and 40 PCA dimensions (Hao et al., 2021; Stuart et al., 2019). The pipeline
493 included QC and data filtration, identification of highly variable genes, dimensional reduction,
494 graph-based clustering, and differential expression analysis for the identification of cluster
495 markers. Each dataset was preprocessed and analyzed separately at first, and later integrated
496 with anchor-based batch correction. Further sample details and photographs are in
497 Supplementary Materials and Methods.

498

499 Integration of heart scRNA-seq and snRNA-seq datasets

500 We integrated our dataset (snRNA-seq) with scRNA-seq datasets of human heart from early
501 stages using the top 1000 HVGs and reciprocal PCA (RPCA) in Seurat; specifically, the
502 datasets included CS12-16 (Xu et al., 2023) and 6.5-7 post-conceptional weeks (Asp et al.,
503 2019). The similarity between cell types across datasets was defined as 1/(1 + distance),
504 where the distance between cell types was determined using a Mehalanobis-like distance
505 metric in Slingshot (Street et al., 2018) based on the top 30 principal components (PCs) of the
506 integrated dataset. Cell types were matched between adjacent developmental stages. The
507 best-matching cell type was initially linked if similarity > 0.06. A secondary match was linked
508 if the similarity z-score across all cell types was > 1 and similarity > 0.06.

Integration of cardiomyocyte and stromal cells from three datasets

The UMI count matrices of cardiomyocyte and stromal cells from each dataset were combined in Seurat. Integration was performed using the top 1000 HVGs and RPCA, followed by reclustering with top 30 PCs and resolution 0.4. Sixteen clusters were obtained in reclustering for cardiomyocyte and stromal cells across three datasets. PHATE analysis (Moon et al., 2019) was performed on the cardiomyocyte and stromal cells using PCA input and 20 KNNs (k-nearest neighbors). Clusters identified during reclustering were mapped onto the PHATE embedding. The trajectories of those clusters were computed using Slingshot [PmID 29914354] with PCA input.

To classify gene expression along the bifurcation of CmF, we defined four distinct patterns: (1) CmMit > Fb3 and CmF > Fb3; (2) CmMit > CmF and CmMit > Fb3; (3) CmMit < CmF and CmMit < Fb3; (4) CmMit < Fb3 and CmF < Fb3. Here, the '<' and '>' were defined by at least 2-fold change and mean expression > 0.5.

Spatial transcriptomics

Fresh fetal hearts were staged, photographed under a Leica dissecting microscope and flash-frozen in Leica Frozen Section Compound (FSC)22 in polypropylene molds floated over isopentane cooled by liquid nitrogen. Blocks were stored at -80°C pending quality control (staging, sexing and euploidy). One male heart at 8.4 pcw (HEF_DN_F0000476) and a female heart at 9.7 pcw (HEF_DN_F0000298) were selected. Blocks were trimmed, sectioned at 10 µm and slices melted onto one of: a 10X Genomics Tissue Optimization Slide to determine optimal time for protease digestion (18 minutes); Superfrost Plus (Menzel Gläser) slides for subsequent validation; or a Visium v1 Spatial Gene Expression slide (10X Genomics, one individual heart per slide, with 55 µm spots arrayed at 100 µm center-to-center distance). All were stored with desiccant at -20°C until further processing. As per the Visium v1 Gene Expression protocol, sections were stained in hematoxylin/eosin (H&E), imaged at 10X on an AxioScan 7 (Zeiss, MMG imaging platform), then barcoded mRNA content was captured to generate DNA libraries. Sequencing of libraries was done by the GBiM platform as above.

After standard quality control, reads were aligned to the human reference genome (GRCh38-2020-A) with SpaceRanger v2.0.1 to generate a UMI count matrix per spot. Spots overlaid by tissue were designated from the H&E scans using the manual alignment tool from Loupe Browser v6.4.1 (10X Genomics) to retain only tissue-associated barcodes. Two poorly

542 adherent tissue slices of the 8.4 pcw heart were excluded from further analyses. Two (A90-
543 A91) and four slices (A17-A20) of the younger and older hearts were retained for further
544 analysis and respectively had >3000 median UMI counts per spot under tissue.

545 *Analysis, visualization and integration of spatial transcriptomic datasets*

546 Spatial transcriptomic data were first explored by individual section using Loupe v8.0 (10X
547 Genomics) and in further depth with Seurat v5.0.3 (Hao et al., 2024) using 30 dimensions.
548 Clusters were obtained by applying resolutions of 0.45 (section A17), 0.65 (A18), 0.35 (A19),
549 0.20 (A20), 0.30 (A90) and 0.35 (A91). The R package 'scTransform' was used for
550 normalization and variance stabilization (Hafemeister and Satija, 2019). After individual slices
551 were examined and compared, data were integrated using Seurat v5.0.3, spots re-clustered
552 at 0.47 resolution, and clusters manually annotated based on prior knowledge of markers and
553 anatomy.

554

555 *Spatial transcriptomic data deconvolution*

556 RCTD (robust cell-type decomposition (Cable et al., 2022)) from the 'SpaceX' (spatially
557 dependent gene co-expression network) R package was used to deconvolute spatial
558 transcriptomic data. Using our integrated snRNAseq data as a reference, we mapped the 21
559 identified cell types to their spatial distributions on each section. The RCTD "full mode" was
560 used to assign any number of cell types per spot of spatial transcriptomic data. Cell-type
561 weights for each slice, which represent the estimated proportion of each cell type for each
562 spot, were assigned and normalized to sum to 1. This was represented in the form of pie
563 charts for each spot and projected on to the spatial transcriptomic section images to show the
564 estimated proportions of each cell type per spot. CmMit was manually excluded from the
565 snRNAseq reference for deconvolution as it prevented visualization of the true cell type
566 heterogeneity in each spot with strong expression of generic genes as *MYH6* and *MYH7,*
567 *TOP2A*, *MT-CO1* and *COL1A2*, masking other cell types in the other groups.

568 Functional analyses of term annotations

569 Enrichr-KG (Evangelista et al., 2023) analyses of gene lists were annotated by terms from
570 2021-2022 releases of the Descartes human fetal atlas (Cao et al., 2020), the Human Gene
571 Atlas (Mabbott et al., 2013), the Tabula Sapiens (The Tabula Sapiens Consortium, 2022)
572 Gene Ontology Biological Processes, and the Kyoto Encyclopedia of Genes and Genomes
573 (KEGG) Human Gene and Pathway databases. Boolean operations on lists of genes were

574 made with GeneVenn (Pirooznia et al., 2007) and/or “Draw Venn Diagrams” (Vandepeer,
575 2011).

576 Histology

577 *Hematoxylin and eosin staining*

578 Heart formalin-fixed, paraffin-embedded (FFPE) sections were deparaffinized twice in xylene
579 and progressively rehydrated in ethanol baths of decreasing concentrations diluted in H_2O.
580 Rehydrated sections were incubated in Mayer’s hematoxylin (Sigma-Aldrich, MHS32) for 2
581 minutes, rinsed in H_2O, differentiated briefly in Acid Alcohol (Sigma-Aldrich, A3179), rinsed
582 again for 2 minutes then incubated 5 minutes in aqueous eosin Y (Sigma-Aldrich, HT110232).
583 Sections were dehydrated then mounted with EuKitt (Sigma-Aldrich, 03989). Heart sections
584 were imaged using a Zeiss AxioScan Z1.

585 Immunofluorescence

586 *Immunofluorescence on cryosection*

587 Hearts were collected in 1X PBS at 4°C and fixed in 4% aqueous buffered paraformaldehyde
588 in PBS (PFA, Electron Microscopy Sciences, 15714) overnight. Hearts were then rinsed in 1X
589 PBS and placed in 15% followed by 30% sucrose in 1X PBS until equilibration at 4°C. Hearts
590 were embedded in OCT (Optimal Cutting Temperature compound, Leica Biosystems,
591 3801480), oriented, flash-frozen over dry ice or liquid nitrogen and stored at -80°C. Hearts
592 were sectioned to 10 µm thickness using a Leica cryostat. Sections were washed in 1X PBS
593 and fixed 10 minutes in 2% PFA. Sections were permeabilized in 0.1% Triton X-100 (Sigma-
594 Aldrich) in PBS for 20 minutes then incubated in an excess of blocking solution (1% bovine
595 serum albumin, Sigma-Aldrich, A7906; 1% inactivated horse serum, GE Healthcare B15-023;
596 0.1% Tween-20, Sigma-Aldrich, P1379; in 1X PBS) for 1h. Sections were incubated with
597 primary antibodies diluted in blocking solution overnight at 4°C. After rinsing in PBS, heart
598 sections were incubated with secondary antibodies (Invitrogen, ThermoFisher Scientific)
599 diluted to 1/500 in blocking solution containing 300 nM DAPI (4',6-diamidino-2-phénylindole)
600 at room temperature for 2 hours. After washes in 1X PBS, slides were mounted in
601 Fluoromount-G (ThermoFisher Scientific, 00-4958-02). Sections were imaged using a Zeiss
602 LSM800 confocal microscope or a Zeiss AxioImager Z2 stereomicroscope with an ApoTome
603 device.

604 Rabbit anti-ALDH1A1 from GeneTex (GTX123973) and rabbit anti-CRABP2 (Sigma,
605 HPA004135) were diluted to 1/100. Mouse anti-MYL7 (also known as MLC-2A, Synaptic

606 Systems, 311011) was used at 1/200. Mouse anti-MYH6 (Sigma, AMAb90950) and mouse
607 anti-MYH7 (Abcam ab207926) were diluted to 1/500. Highly cross-absorbed secondary
608 antibodies against relevant species, coupled to AlexaFluor-488, -555 or -647, were all
609 purchased from Thermo Fisher Scientific (refs A11008, A11029, A21244, A31572, A31570,
610 A32787). They were diluted to 1/500 in blocking solution with 300 nM DAPI (4′,6-diamidino-2-
611 phenylindole), and applied to sections for 1h before rinsing.

612

613 *Immunofluorescence on whole hearts*

614 Hearts were collected in cold HBSS, rinsed in PBS and fixed 1 hour in PFA at 4°C with gentle
615 agitation. After washes in 1X PBS, hearts were dehydrated at room temperature 50%, 80%
616 and 100% methanol for 1.5 hour each under agitation. Hearts were then incubated overnight
617 at 4°C in 80% methanol, 6% H_2O_2. After progressive rehydration, hearts were incubated in
618 PBSGT (0.2% porcine skin gelatin [VWR 24350.262], 0.5% Triton X-100, 0.01% sodium azide
619 [Sigma-Aldrich, S2002] in 1X PBS) for 3 days with gentle agitation at room temperature.
620 Hearts were then incubated with primary antibodies against CD31/PECAM1 (Cell Signaling
621 Technology, #3528, clone 89C2 at 1/200) and PRPH1 (Sigma-Aldrich AB1530, at 1/1000) at
622 37°C for 17 to 24 days proportional to relative size, with constant mild agitation. Alternatively,
623 they were incubated in antibodies against ALDH1A1 (Abcam ab52492 clone EP1933Y),
624 S100B (GeneTex GTX14849 clone 4B3), EGR2 (Millipore ABE1374), FABP4 (Bioss BSM-
625 51247M clone 5C1), POSTN (Origene TA804575S clone OTI2B2), or MYH6 (Sigma-Aldrich
626 AMAb90950 clone CL2162). After 24h of washing in six or more changes of PBT (0.5% Triton-
627 X100 in 1X PBS), hearts were incubated with secondary antibodies diluted to 1/1000
628 (ThermoFisher Scientific, Invitrogen) in PBSGT for 2 days at 37°C. After six or more washes
629 in PBT, hearts were dehydrated. After progressive dehydration in methanol, anhydrous hearts
630 were incubated overnight in brown glass vials with two parts dichloromethane (Sigma-Aldrich,
631 270997, CAS 75-09-2) to one part methanol until settling, followed by 100% dichloromethane
632 to equilibration. Hearts were next incubated in 100% (di)benzyl ether (Sigma-Aldrich, 108014,
633 CAS 103-50-4) for at least 7 hours (Belle et al., 2017). Transparent hearts were conserved in
634 benzyl ether but transferred to ethyl cinnamate (Sigma-Aldrich, 112372, CAS 103-36-6) for
635 imaging with a Blaze light-sheet UltraMicroscope (Miltenyi Biotec). Imaris software (Oxford
636 Instruments) was used to reconstruct 3D images.

637 RNAscope *in situ* hybridization on paraffin sections

638 Hearts were collected in cold 1X PBS and fixed overnight in 4% PFA. Hearts were then rinsed
639 in 1X PBS and dehydrated in progressive ethanol baths until complete dehydration in 100%

640 ethanol, equilibrated to xylene (twice, 1 hour each), embedded in paraffin and stored at 4°C.
641 10 µm sections were made using a microtome and mounted on SuperFrost Ultra Plus GOLD
642 slides (Microm Microtech, Epredia, K5800AMNZ72). RNAscope *in situ* hybridization was
643 performed using the RNAscope Multiplex Fluorescent v2 kit from Advanced Cell Diagnostics
644 (ACD), following the manufacturer's protocol. Before the probe hybridization step, sections
645 were incubated in the "protease PLUS" solution for 15 minutes at 40°C. Up to three of *CRABP1*
646 (855321-C2), *ISL1* (478591-C3), *PRRX1* (511001-C2), *PENK* (548301-C3), *MEOX1*
647 (564321), *ACTA1* (454311) and *BMP10* (459641) RNAscope probes were then hybridized.
648 Nuclei were counterstained with the provided DAPI solution. Opal 520, Opal 570 and/or Opal
649 690 reagent packs (Akoya Biosciences) were used at 1/200 dilution to localize probes. Heart
650 sections were imaged with tiling on a Zeiss LSM800 confocal microscope and stitched with
651 Zen 3.7 software.

652 Websites

653 Loupe Browser

654 https://www.10xgenomics.com/products/loupe-browser/downloads/eula

655 Seurat vignettes and use-cases

656 https://satijalab.org/seurat/articles/pbmc3k_tutorial

657 https://satijalab.org/seurat/articles/sctransform_vignette

658 https://satijalab.org/seurat/articles/spatial_vignette

659 Enrichr-KG

660 https://maayanlab.cloud/enrichr-kg

661 Venn diagrams and subsets of co-expression

662 https://www.bioinformatics.org/gvenn/

663 https://bioinformatics.psb.ugent.be/webtools/Venn/

664 Human Developmental Cell Atlas (France)

665 https://hudeca.com/

666 https://hudeca.genouest.org/

References

Alexanian, M., Przytycki, P. F., Micheletti, R., Padmanabhan, A., Ye, L., Travers, J. G., Gonzalez-Teran, B., Silva, A. C., Duan, Q., Ranade, S. S., et al. (2021). A transcriptional switch governs fibroblast activation in heart disease. *Nature* 595, 438–443.

Ali, S. R., Ranjbarvaziri, S., Talkhabi, M., Zhao, P., Subat, A., Hojjat, A., Kamran, P., Müller, A. M. S., Volz, K. S., Tang, Z., et al. (2014). Developmental heterogeneity of cardiac fibroblasts does not predict pathological proliferation and activation. *Circ. Res.* 115, 625–635.

Anderson, R. H., Webb, S., Brown, N. A., Lamers, W. and Moorman, A. (2003). Development of the Heart: (1) Formation of the Cardiac Chambers and Arterial Trunks. *Heart* 89, 806–814.

Argiro, L., Chevalier, C., Choquet, C., Nandkishore, N., Ghata, A., Baudot, A., Zaffran, S. and Lescroart, F. (2024). Gastruloids are competent to specify both cardiac and skeletal muscle lineages. *Nat. Commun.* 15, 10172.

Asp, M., Giacomello, S., Larsson, L., Wu, C., Fürth, D., Qian, X., Wärdell, E., Custodio, J., Reimegård, J., Salmén, F., et al. (2019). A Spatiotemporal Organ-Wide Gene Expression and Cell Atlas of the Developing Human Heart. *Cell* 179, 1647-1660.e19.

Assou, S., Girault, N., Plinet, M., Bouckenheimer, J., Sansac, C., Combe, M., Mianné, J., Bourguignon, C., Fieldes, M., Ahmed, E., et al. (2020). Recurrent Genetic Abnormalities in Human Pluripotent Stem Cells: Definition and Routine Detection in Culture Supernatant by Targeted Droplet Digital PCR. *Stem Cell Rep.* 14, 1–8.

Bayraktar, S., Cranley, J., Kanemaru, K., Knight-Schrijver, V., Colzani, M., Davaapil, H., Lee, J. C. M., Polanski, K., Richardson, L., Semprich, C. I., et al. (2024). High-resolution atlas of the developing human heart and the great vessels. 2024.04.27.591127.

Belle, M., Godefroy, D., Couly, G., Malone, S. A., Collier, F., Giacobini, P. and Chédotal, A. (2017). Tridimensional Visualization and Analysis of Early Human Development. *Cell* 169, 161-173.e12.

Bergmann, O., Bhardwaj, R. D., Bernard, S., Zdunek, S., Barnabé-Heider, F., Walsh, S., Zupicich, J., Alkass, K., Buchholz, B. A., Druid, H., et al. (2009). Evidence for cardiomyocyte renewal in humans. *Science* 324, 98.

Blain, R., Couly, G., Shotar, E., Blévinal, J., Toupin, M., Favre, A., Abjaghou, A., Inoue, M., Hernández-Garzón, E., Clarençon, F., et al. (2023). A tridimensional atlas of the developing human head. *Cell* 186, 5910-5924.e17.

Blair, E., Redwood, C., Ashrafian, H., Oliveira, M., Broxholme, J., Kerr, B., Salmon, A., Ostman-Smith, I. and Watkins, H. (2001). Mutations in the gamma(2) subunit of AMP-activated protein kinase cause familial hypertrophic cardiomyopathy: evidence for the central role of energy compromise in disease pathogenesis. *Hum. Mol. Genet.* 10, 1215–1220.

Boeva, V., Louis-Brennetot, C., Peltier, A., Durand, S., Pierre-Eugène, C., Raynal, V., Etchevers, H. C., Thomas, S., Lermine, A., Daudigeos-Dubus, E., et al. (2017).

Heterogeneity of neuroblastoma cell identity defined by transcriptional circuitries. *Nat. Genet.* 49, 1408–1413.

Boppana, A., Lee, S., Malhotra, R., Halushka, M., Gustilo, K. S., Quardokus, E. M., Herr, B. W., Börner, K. and Weber, G. M. (2023). Anatomical structures, cell types, and biomarkers of the healthy human blood vasculature. *Sci. Data* 10, 452.

Butler, A., Hoffman, P., Smibert, P., Papalexi, E. and Satija, R. (2018). Integrating single-cell transcriptomic data across different conditions, technologies, and species. *Nat. Biotechnol.* 36, 411–420.

Cable, D. M., Murray, E., Zou, L. S., Goeva, A., Macosko, E. Z., Chen, F. and Irizarry, R. A. (2022). Robust decomposition of cell type mixtures in spatial transcriptomics. *Nat. Biotechnol.* 40, 517–526.

Cao, J., O'Day, D. R., Pliner, H. A., Kingsley, P. D., Deng, M., Daza, R. M., Zager, M. A., Aldinger, K. A., Blecher-Gonen, R., Zhang, F., et al. (2020). A human cell atlas of fetal gene expression. *Science* 370, eaba7721.

Chen, H., Shi, S., Acosta, L., Li, W., Lu, J., Bao, S., Chen, Z., Yang, Z., Schneider, M. D., Chien, K. R., et al. (2004). BMP10 is essential for maintaining cardiac growth during murine cardiogenesis. *Dev. Camb. Engl.* 131, 2219–2231.

Chen, T., Song, S., Jiang, H., Lian, H. and Hu, S. (2022). Single Cell Sequencing Reveals Mechanisms of Persistent Truncus Arteriosus Formation after PDGFRα and PDGFRβ Double Knockout in Cardiac Neural Crest Cells. *Genes* 13, 1708.

Clay, M. R. and Halloran, M. C. (2014). Cadherin 6 promotes neural crest cell detachment via F-actin regulation and influences active Rho distribution during epithelial-to-mesenchymal transition. *Dev. Camb. Engl.* 141, 2506–2515.

Cranley, J., Kanemaru, K., Bayraktar, S., Knight-Schrijver, V., Pett, J. P., Polanski, K., Dabrowska, M., Mulas, I., Richardson, L., Semprich, C., et al. (2024). Multiomic analysis reveals developmental dynamics of the human heart in health and disease. 2024.04.29.591736.

D'Antonio, M., Nguyen, J. P., Arthur, T. D., Matsui, H., Donovan, M. K. R., D'Antonio-Chronowska, A. and Frazer, K. A. (2022). In heart failure reactivation of RNA-binding proteins is associated with the expression of 1,523 fetal-specific isoforms. *PLoS Comput. Biol.* 18, e1009918.

Deng, Y., He, Y., Xu, J., He, H. and Li, G. (2023). Heterogeneity and Functional Analysis of Cardiac Fibroblasts in Heart Development. *BioRxiv Prepr. Serv. Biol.* 2023.07.30.551164.

Dettman, R. W., Denetclaw, W., Ordahl, C. P. and Bristow, J. (1998). Common epicardial origin of coronary vascular smooth muscle, perivascular fibroblasts, and intermyocardial fibroblasts in the avian heart. *Dev. Biol.* 193, 169–81.

Dewing, J. M., Saunders, V., O'Kelly, I. and Wilson, D. I. (2022). Defining cardiac cell populations and relative cellular composition of the early fetal human heart. *PLOS ONE* 17, e0259477.

El Robrini, N., Etchevers, H. C., Ryckebüsch, L., Faure, E., Eudes, N., Niederreither, K., Zaffran, S. and Bertrand, N. (2016). Cardiac outflow morphogenesis depends on effects of retinoic acid signaling on multiple cell lineages. *Dev. Dyn.* 245, 388–401.

Etchevers, H. C., Vincent, C., Le Douarin, N. M. and Couly, G. F. (2001). The cephalic neural crest provides pericytes and smooth muscle cells to all blood vessels of the face and forebrain. *Development* 128, 1059–68.

Evangelista, J. E., Xie, Z., Marino, G. B., Nguyen, N., Clarke, D. J. B. and Ma'ayan, A. (2023). Enrichr-KG: bridging enrichment analysis across multiple libraries. *Nucleic Acids Res.* 51, W168–W179.

Evtouchenko, L., Studer, L., Spenger, C., Dreher, E. and Seiler, R. W. (1996). A mathematical model for the estimation of human embryonic and fetal age. *Cell Transplant.* 5, 453–464.

Farah, E. N., Hu, R. K., Kern, C., Zhang, Q., Lu, T.-Y., Ma, Q., Tran, S., Zhang, B., Carlin, D., Monell, A., et al. (2024). Spatially organized cellular communities form the developing human heart. *Nature* 627, 854–864.

Fukada, M., Fujikawa, A., Chow, J. P. H., Ikematsu, S., Sakuma, S. and Noda, M. (2006). Protein tyrosine phosphatase receptor type Z is inactivated by ligand-induced oligomerization. *FEBS Lett.* 580, 4051–4056.

Gaussin, V., Morley, G. E., Cox, L., Zwijsen, A., Vance, K. M., Emile, L., Tian, Y., Liu, J., Hong, C., Myers, D., et al. (2005). Alk3/Bmpr1a receptor is required for development of the atrioventricular canal into valves and annulus fibrosus. *Circ. Res.* 97, 219–226.

George, D., Ahrens, P. and Lambert, S. (2018). Satellite glial cells represent a population of developmentally arrested Schwann cells. *Glia* 66, 1496–1506.

Gerrelli, D., Lisgo, S., Copp, A. J. and Lindsay, S. (2015). Enabling research with human embryonic and fetal tissue resources. *Dev. Camb. Engl.* 142, 3073–3076.

Gittenberger-de Groot, A. C., Vrancken Peeters, M. P., Mentink, M. M., Gourdie, R. G. and Poelmann, R. E. (1998). Epicardium-derived cells contribute a novel population to the myocardial wall and the atrioventricular cushions. *Circ. Res.* 82, 1043–1052.

Gollob, M. H., Seger, J. J., Gollob, T. N., Tapscott, T., Gonzales, O., Bachinski, L. and Roberts, R. (2001). Novel PRKAG2 mutation responsible for the genetic syndrome of ventricular preexcitation and conduction system disease with childhood onset and absence of cardiac hypertrophy. *Circulation* 104, 3030–3033.

Guo, X.-J., Qiu, X.-B., Wang, J., Guo, Y.-H., Yang, C.-X., Li, L., Gao, R.-F., Ke, Z.-P., Di, R.-M., Sun, Y.-M., et al. (2021). PRRX1 Loss-of-Function Mutations Underlying Familial Atrial Fibrillation. *J. Am. Heart Assoc.* 10, e023517.

Hafemeister, C. and Satija, R. (2019). Normalization and variance stabilization of single-cell RNA-seq data using regularized negative binomial regression. *Genome Biol.* 20, 296.

Hailstones, D., Barton, P., Chan-Thomas, P., Sasse, S., Sutherland, C., Hardeman, E. and Gunning, P. (1992). Differential regulation of the atrial isoforms of the myosin light chains during striated muscle development. *J. Biol. Chem.* 267, 23295–23300.

Haniffa, M., Taylor, D., Linnarsson, S., Aronow, B. J., Bader, G. D., Barker, R. A., Camara, P. G., Camp, J. G., Chédotal, A., Copp, A., et al. (2021). A roadmap for the Human Developmental Cell Atlas. *Nature* 597, 196–205.

Hao, Y., Hao, S., Andersen-Nissen, E., Mauck, W. M., Zheng, S., Butler, A., Lee, M. J., Wilk, A. J., Darby, C., Zager, M., et al. (2021). Integrated analysis of multimodal single-cell data. *Cell* 184, 3573-3587.e29.

Hao, Y., Stuart, T., Kowalski, M. H., Choudhary, S., Hoffman, P., Hartman, A., Srivastava, A., Molla, G., Madad, S., Fernandez-Granda, C., et al. (2024). Dictionary learning for integrative, multimodal and scalable single-cell analysis. *Nat. Biotechnol.* 42, 293–304.

Hern, W. M. (1984). Correlation of fetal age and measurements between 10 and 26 weeks of gestation. *Obstet. Gynecol.* 63, 26–32.

Hikspoors, J. P. J. M., Kruepunga, N., Mommen, G. M. C., Köhler, S. E., Anderson, R. H. and Lamers, W. H. (2022). A pictorial account of the human embryonic heart between 3.5 and 8 weeks of development. *Commun. Biol.* 5, 1–22.

Hill, M. C., Kadow, Z. A., Li, L., Tran, T. T., Wythe, J. D. and Martin, J. F. (2019). A cellular atlas of Pitx2-dependent cardiac development. *Development* 146, dev180398.

Ho, S. Y., Anderson, R. H. and Sánchez-Quintana, D. (2002). Atrial structure and fibres: morphologic bases of atrial conduction. *Cardiovasc. Res.* 54, 325–336.

Hou, X., Si, X., Xu, J., Chen, X., Tang, Y., Dai, Y. and Wu, F. (2024). Single-cell RNA sequencing reveals the gene expression profile and cellular communication in human fetal heart development. *Dev. Biol.* 514, 87–98.

Hulin, A., Hortells, L., Gomez-Stallons, M. V., O'Donnell, A., Chetal, K., Adam, M., Lancellotti, P., Oury, C., Potter, S. S., Salomonis, N., et al. (2019). Maturation of heart valve cell populations during postnatal remodeling. *Development* 146, dev173047.

Jiang, X., Rowitch, D. H., Soriano, P., McMahon, A. P. and Sucov, H. M. (2000). Fate of the mammalian cardiac neural crest. *Development* 127, 1607–1616.

Jiang, X., Lian, X., Wei, K., Zhang, J., Yu, K., Li, H., Ma, H., Cai, Y. and Pang, L. (2024). Maturation of pluripotent stem cell-derived cardiomyocytes: limitations and challenges from metabolic aspects. *Stem Cell Res. Ther.* 15, 354.

Jin, S., Plikus, M. V. and Nie, Q. (2024). CellChat for systematic analysis of cell–cell communication from single-cell transcriptomics. *Nat. Protoc.* 1–40.

Kahr, P. C., Piccini, I., Fabritz, L., Greber, B., Schöler, H., Scheld, H. H., Hoffmeier, A., Brown, N. A. and Kirchhof, P. (2011). Systematic analysis of gene expression differences between left and right atria in different mouse strains and in human atrial tissue. *PloS One* 6, e26389.

Kaltenecker, D., Al-Maskari, R., Negwer, M., Hoeher, L., Kofler, F., Zhao, S., Todorov, M., Rong, Z., Paetzold, J. C., Wiestler, B., et al. (2024). Virtual reality-empowered deep-learning analysis of brain cells. *Nat. Methods* 21, 1306–1315.

Kanemaru, K., Cranley, J., Muraro, D., Miranda, A. M. A., Ho, S. Y., Wilbrey-Clark, A., Patrick Pett, J., Polanski, K., Richardson, L., Litvinukova, M., et al. (2023). Spatially resolved multiomics of human cardiac niches. *Nature* 619, 801–810.

Ke, Z.-P., Zhang, G.-F., Guo, Y.-H., Sun, Y.-M., Wang, J., Li, N., Qiu, X.-B., Xu, Y.-J. and Yang, Y.-Q. (2022). A novel PRRX1 loss-of-function variation contributing to familial atrial fibrillation and congenital patent ductus arteriosus. *Genet. Mol. Biol.* 45, e20210378.

Knight-Schrijver, V. R., Davaapil, H., Bayraktar, S., Ross, A. D. B., Kanemaru, K., Cranley, J., Dabrowska, M., Patel, M., Polanski, K., He, X., et al. (2022). A single-cell comparison of adult and fetal human epicardium defines the age-associated changes in epicardial activity. *Nat. Cardiovasc. Res.* 1, 1215–1229.

Kostina, A., Kiselev, A., Huang, A., Lankerd, H., Caywood, S., Jurado-Fernandez, A., Volmert, B., O'Hern, C., Juhong, A., Liu, Y., et al. (2024). Self-organizing human heart assembloids with autologous and developmentally relevant cardiac neural crest-derived tissues. 2024.12.11.627627.

Krane, M., Dreßen, M., Santamaria, G., My, I., Schneider, C. M., Dorn, T., Laue, S., Mastantuono, E., Berutti, R., Rawat, H., et al. (2021). Sequential Defects in Cardiac Lineage Commitment and Maturation Cause Hypoplastic Left Heart Syndrome. *Circulation* 144, 1409–1428.

Lalani, S. R., Thakuria, J. V., Cox, G. F., Wang, X., Bi, W., Bray, M. S., Shaw, C., Cheung, S. W., Chinault, A. C., Boggs, B. A., et al. (2009). 20p12.3 microdeletion predisposes to Wolff-Parkinson-White syndrome with variable neurocognitive deficits. *J. Med. Genet.* 46, 168–175.

Lardenois, A., Suglia, A., Moore, C., Evrard, B., Noël, L., Rivaud, P., Besson, A., Toupin, M., Léonard, S., Lesné, L., et al. (2023). Single-cell transcriptome landscape of developing fetal gonads defines somatic cell lineage specification in humans. 2023.08.07.552336.

Lázár, E., Mauron, R., Andrusivová, Ž., Foyer, J., He, M., Larsson, L., Shakari, N., Salas, S. M., Avenel, C., Sariyar, S., et al. (2024). Spatial Dynamics of the Developing Human Heart. 2024.03.12.584577.

Le Lièvre, C. S. and Le Douarin, N. M. (1975). Mesenchymal derivatives of the neural crest: analysis of chimaeric quail and chick embryos. *J. Embryol. Exp. Morphol.* 34, 125–154.

Lee, K.-W., Yeo, S.-Y., Gong, J.-R., Koo, O.-J., Sohn, I., Lee, W. Y., Kim, H. C., Yun, S. H., Cho, Y. B., Choi, M.-A., et al. (2022). PRRX1 is a master transcription factor of stromal fibroblasts for myofibroblastic lineage progression. *Nat. Commun.* 13, 2793.

Lescroart, F., Chabab, S., Lin, X., Rulands, S., Paulissen, C., Rodolosse, A., Auer, H., Achouri, Y., Dubois, C., Bondue, A., et al. (2014). Early lineage restriction in temporally distinct populations of Mesp1 progenitors during mammalian heart development. *Nat. Cell Biol.* 16, 829–840.

Leshem, R., Baker, S. M., Mallen, J., Wang, L., Dark, J., Sharrocks, A. D., Hanley, K. P., Hanley, N. A., Rattray, M., Bamforth, S. D., et al. (2024). A cell atlas of the developing human outflow tract of the heart and its adult derivatives. 2023.04.05.535627.

Lewis-Israeli, Y. R., Wasserman, A. H., Gabalski, M. A., Volmert, B. D., Ming, Y., Ball, K. A., Yang, W., Zou, J., Ni, G., Pajares, N., et al. (2021). Self-assembling human heart organoids for the modeling of cardiac development and congenital heart disease. *Nat. Commun.* 12, 5142.

Litviňuková, M., Talavera-López, C., Maatz, H., Reichart, D., Worth, C. L., Lindberg, E. L., Kanda, M., Polanski, K., Heinig, M., Lee, M., et al. (2020). Cells of the adult human heart. *Nature* 588, 466–472.

Liu, C., Liu, W., Palie, J., Lu, M. F., Brown, N. a and Martin, J. F. (2002). Pitx2c patterns anterior myocardium and aortic arch vessels and is required for local cell movement into atrioventricular cushions. *Development* 129, 5081–91.

Liu, K., Yu, W., Tang, M., Tang, J., Liu, X., Liu, Q., Li, Y., He, L., Zhang, L., Evans, S. M., et al. (2018). A dual genetic tracing system identifies diverse and dynamic origins of cardiac valve mesenchyme. *Development* 145, dev167775.

Liu, X., Chen, W., Li, W., Li, Y., Priest, J. R., Zhou, B., Wang, J. and Zhou, Z. (2019). Single-Cell RNA-Seq of the Developing Cardiac Outflow Tract Reveals Convergent Development of the Vascular Smooth Muscle Cells. *Cell Rep.* 28, 1346-1361.e4.

Liu, K., Jin, H., Zhang, S., Tang, M., Meng, X., Li, Y., Pu, W., Lui, K. O. and Zhou, B. (2023). Intercellular genetic tracing of cardiac endothelium in the developing heart. *Dev. Cell* 58, 1502-1512.e3.

Lu, P., Wu, B., Feng, X., Cheng, W., Kitsis, R. N. and Zhou, B. (2022). Cardiac Myosin Heavy Chain Reporter Mice to Study Heart Development and Disease. *Circ. Res.* 131, 364–366.

Lv, F., Ge, X., Qian, P., Lu, X., Liu, D. and Chen, C. (2022). Neuron navigator 3 (NAV3) is required for heart development in zebrafish. *Fish Physiol. Biochem.* 48, 173–183.

Mabbott, N. A., Baillie, J. K., Brown, H., Freeman, T. C. and Hume, D. A. (2013). An expression atlas of human primary cells: inference of gene function from coexpression networks. *BMC Genomics* 14, 632.

Maldonado, E., Rangel-Huerta, E., González-Gómez, R., Fajardo-Alvarado, G. and Morillo-Velarde, P. S. (2019). Octopus insularis as a new marine model for evolutionary developmental biology. *Biol. Open* 8, bio046086.

Martelotto, L. G. (2021). S.O.F protocol for nuclei isolation from fresh and frozen tissues using OptiPrep® discontinuous gradient V.4.

McKellar, D. W., Walter, L. D., Song, L. T., Mantri, M., Wang, M. F. Z., De Vlaminck, I. and Cosgrove, B. D. (2021). Large-scale integration of single-cell transcriptomic data captures transitional progenitor states in mouse skeletal muscle regeneration. *Commun. Biol.* 4, 1280.

Moon, K. R., van Dijk, D., Wang, Z., Gigante, S., Burkhardt, D. B., Chen, W. S., Yim, K., Elzen, A. van den, Hirn, M. J., Coifman, R. R., et al. (2019). Visualizing structure and transitions in high-dimensional biological data. *Nat. Biotechnol.* 37, 1482–1492.

Muhl, L., Genové, G., Leptidis, S., Liu, J., He, L., Mocci, G., Sun, Y., Gustafsson, S., Buyandelger, B., Chivukula, I. V., et al. (2020). Single-cell analysis uncovers fibroblast heterogeneity and criteria for fibroblast and mural cell identification and discrimination. *Nat. Commun.* 11, 1–18.

Norris, R. A., Potts, J. D., Yost, M. J., Junor, L., Brooks, T., Tan, H., Hoffman, S., Hart, M. M., Kern, M. J., Damon, B., et al. (2009). Periostin promotes a fibroblastic lineage pathway in atrioventricular valve progenitor cells. *Dev. Dyn.* 238, 1052–63.

Nowotschin, S., Liao, J., Gage, P. J., Epstein, J. A., Campione, M. and Morrow, B. E. (2006). Tbx1 affects asymmetric cardiac morphogenesis by regulating Pitx2 in the secondary heart field. *Dev. Camb. Engl.* 133, 1565–73.

Oetjen, S., Mahlke, C., Hermans-Borgmeyer, I. and Hermey, G. (2014). Spatiotemporal expression analysis of the growth factor receptor SorCS3. *J. Comp. Neurol.* 522, 3386–3402.

O'Rahilly, R. (1971). The timing and sequence of events in human cardiogenesis. *Acta Anat. (Basel)* 79, 70–75.

O'Rahilly, R. and Müller, F. (1987). *Developmental Stages in Humans: including a revision of Streeter's "Horizons" and a survey of the Carnegie collection*. Washington, D.C.: Carnegie Institution of Washington.

O'Rahilly, R. and Müller, F. (2010). Developmental stages in human embryos: revised and new measurements. *Cells Tissues Organs* 192, 73–84.

Pirooznia, M., Nagarajan, V. and Deng, Y. (2007). GeneVenn - A web application for comparing gene lists using Venn diagrams. *Bioinformation* 1, 420–422.

Ramesh, N., Escher, M. J. F., Mampell, M. M., Böhme, M. A., Götz, T. W. B., Goel, P., Matkovic, T., Petzoldt, A. G., Dickman, D. and Sigrist, S. J. (2021). Antagonistic interactions between two Neuroligins coordinate pre- and postsynaptic assembly. *Curr. Biol. CB* 31, 1711-1725.e5.

Sacks, H. S. and Fain, J. N. (2007). Human epicardial adipose tissue: a review. *Am. Heart J.* 153, 907–917.

Sedmera, D., Pexieder, T., Vuillemin, M., Thompson, R. P. and Anderson, R. H. (2000). Developmental patterning of the myocardium. *Anat. Rec.* 258, 319–337.

Smirnov, A. V., Kontsevaya, G. V., Feofanova, N. A., Anisimova, M. V., Serova, I. A., Gerlinskaya, L. A., Battulin, N. R., Moshkin, M. P. and Serov, O. L. (2018). Unexpected phenotypic effects of a transgene integration causing a knockout of the endogenous Contactin-5 gene in mice. *Transgenic Res.* 27, 1–13.

Soldatov, R., Kaucka, M., Kastriti, M. E., Petersen, J., Chontorotzea, T., Englmaier, L., Akkuratova, N., Yang, Y., Häring, M., Dyachuk, V., et al. (2019). Spatiotemporal structure of cell fate decisions in murine neural crest. *Science* 364, eaas9536.

Soonpaa, M. H., Kim, K. K., Pajak, L., Franklin, M. and Field, L. J. (1996). Cardiomyocyte DNA synthesis and binucleation during murine development. *Am. J. Physiol.* 271, H2183-2189.

Street, K., Risso, D., Fletcher, R. B., Das, D., Ngai, J., Yosef, N., Purdom, E. and Dudoit, S. (2018). Slingshot: cell lineage and pseudotime inference for single-cell transcriptomics. *BMC Genomics* 19, 477.

Stuart, T., Butler, A., Hoffman, P., Hafemeister, C., Papalexi, E., Mauck, W. M., Hao, Y., Stoeckius, M., Smibert, P. and Satija, R. (2019). Comprehensive Integration of Single-Cell Data. *Cell* 177, 1888-1902.e21.

Su, A. I., Wiltshire, T., Batalov, S., Lapp, H., Ching, K. A., Block, D., Zhang, J., Soden, R., Hayakawa, M., Kreiman, G., et al. (2004). A gene atlas of the mouse and human protein-encoding transcriptomes. *Proc. Natl. Acad. Sci.* 101, 6062–6067.

Tao, G., Kahr, P. C., Morikawa, Y., Zhang, M., Rahmani, M., Heallen, T. R., Li, L., Sun, Z., Olson, E. N., Amendt, B. A., et al. (2016). Pitx2 promotes heart repair by activating the antioxidant response after cardiac injury. *Nature* 534, 119–123.

Teichmann, U. and Kessel, M. (2004). Highly restricted BMP10 expression in the trabeculating myocardium of the chick embryo. *Dev. Genes Evol.* 214, 96–98.

The Tabula Sapiens Consortium (2022). The Tabula Sapiens: A multiple-organ, single-cell transcriptomic atlas of humans. *Science* 376, eabl4896.

van Eif, V. W. W., Stefanovic, S., van Duijvenboden, K., Bakker, M., Wakker, V., de Gier-de Vries, C., Zaffran, S., Verkerk, A. O., Boukens, B. J. and Christoffels, V. M. (2019). Transcriptome analysis of mouse and human sinoatrial node cells reveals a conserved genetic program. *Dev. Camb. Engl.* 146, dev173161.

Vandepeer, Y. (2011). Venn Diagram tool. *Draw Venn Diagr.*

Vrancken Peeters, M.-P. F. M., Gittenberger-de Groot, A. C., Mentink, M. M. T., Poelmann, R. E., Groot, A. C. G., Mentink, M. M. T., Poelmann, R. E., Vrancken Peeters, M.-P. F. M., Gittenberger-de Groot, A. C., Mentink, M. M. T., et al. (1999). Smooth muscle cells and fibroblasts of the coronary arteries derive from epithelial-mesenchymal transformation of the epicardium. *Anat. Embryol. (Berl.)* 199, 367–378.

Waldo, K., Miyagawa-Tomita, S., Kumiski, D. and Kirby, M. L. (1998). Cardiac neural crest cells provide new insight into septation of the cardiac outflow tract: aortic sac to ventricular septal closure. *Dev. Biol.* 196, 129–44.

Wang, H. U., Chen, Z. F. and Anderson, D. J. (1998). Molecular distinction and angiogenic interaction between embryonic arteries and veins revealed by ephrin-B2 and its receptor Eph-B4. *Cell* 93, 741–753.

Wang, J., Klysik, E., Sood, S., Johnson, R. L., Wehrens, X. H. T. and Martin, J. F. (2010). Pitx2 prevents susceptibility to atrial arrhythmias by inhibiting left-sided pacemaker specification. *Proc. Natl. Acad. Sci. U. S. A.* 107, 9753–9758.

Wang, W., Li, X., Ding, X., Xiong, S., Hu, Z., Lu, X., Zhang, K., Zhang, H., Hu, Q., Lai, K. S., et al. (2023). Lymphatic endothelial transcription factor Tbx1 promotes an immunosuppressive microenvironment to facilitate post-myocardial infarction repair. *Immunity* 56, 2342-2357.e10.

White-Brown, A. M., Richard, M., Morency, A.-M., Maedler-Kron, C. and De Bie, I. (2024). PRKAG2-Related Lethal Congenital Glycogen Storage Disease of the Heart as Rare Cause of Fetal Hydrops With Bradycardia and Cardiomyopathy: Clinical Report and Literature Review. *Am. J. Med. Genet. A.* e63865.

Xu, Y., Zhang, T., Zhou, Q., Hu, M., Qi, Y., Xue, Y., Nie, Y., Wang, L., Bao, Z. and Shi, W. (2023). A single-cell transcriptome atlas profiles early organogenesis in human embryos. *Nat. Cell Biol.* 25, 604–615.

Zhao, J., Kennelly, J., Nalar, A., Kulathilaka, A., Sharma, R., Bai, J., Li, N. and Fedorov, V. V. (2023). Chamber-specific wall thickness features in human atrial fibrillation. *Interface Focus* 13, 20230044.

Acknowledgments

Prof. Aubert Agostini and staff of the Centre de Gynécologie Sociale de l'AP-HM in Marseille obtained patient consents and provided most of the tissue donations used in this work, to which effort Maryne Toupin also contributed from Rennes. Laurence Noël built and helped curate the ontologies used in HuDeCA's OpenSpecimen database. The authors gratefully acknowledge personnel of MMG's GBiM and imaging platforms, especially Catherine Robert, Christel Castro, Dr. Valérie Delague, Nicolas Lenfant, Alexandre Atkinson, Deniz Harcanoğlu and Dr. Raphaël Blain for their analysis assistance.

Funding: Institut National de la Santé et de la Recherche Médicale (INSERM) Programme Transversale "HuDeCA", France (MH, YG, AC, SMG, SZ, HCE)

Association Française contre les Myopathies grant "MoThARD" (SK, AB, SZ, HCE)

CDB is supported by a grant from the Fondation pour la Recherche Médicale, France.

This publication is part of the Human Cell Atlas. https://www.humancellatlas.org/publications/

Author contributions:

SZ and HCE conceptualized the study and designed the experiments. CDB, SZ and HCE refined methodology, interpreted the data and wrote the original manuscript draft, to which AB and SK also contributed. MH, MM, WS, CM and SMG processed samples and performed quality control measures. MH carried out the histological, immunofluorescence and high-throughput sequencing-based experiments. CDB, CH, SK, SR, YX, AB and HCE designed, refined and analyzed bioinformatics experiments. AL, IV, YG and AC contributed to the 3D immunofluorescence experimental design, execution and data analyses. CDB, ZB, IV, AC, AB, SZ and HCE supervised the analyses. All authors reviewed and provided input on the final manuscript.

Competing interests: Authors declare that they have no competing interests.

Correspondence and requests for materials should be addressed to heather.etchevers@inserm.fr or stephane.zaffran@inserm.fr

Data and materials availability:

All data, code, and materials used in the analyses are available either in the main text and/or the Supplementary Materials, or deposited in the following repositories: Sequencing data, images and snRNAseq matrices are available from the Gene Expression Omnibus (GEO), https://www.ncbi.nlm.nih.gov/geo/ under accession GSE283967; code from https://github.com/BAUDOTlab/Human_fetal_heart_atlas; movies, large images and high-resolution gross anatomy images are available from Figshare at https://figshare.com/projects/Multi-modal_refinement_of_the_human_heart_atlas_during_the_first_gestational_trimester/213151 . Some images are reproduced at the Human Developmental Biology Resource (UK) fetal cardiac anatomy website (https://bit.ly/HumanFetalHeart).

Human Cell Atlas data from (Xu et al., 2023) is available both at:

https://explore.data.humancellatlas.org/projects/e255b1c6-1143-4fa6-83a8-528f15b41038 and from GEO under accession GSE157329.

710 **Figure legends**

711 Figure 1. Profiling human fetal heart development at the resolution of
712 individual nuclei

713 (**A**) Samples of nuclei were derived from three whole dissociated hearts to generate distinct
714 snRNAseq datasets at 8.6 post-conceptional weeks (pcw, confirmed XX genotype), 9.0 pcw
715 (XY) and 10.7 pcw (XY). Samples of spatial transcriptomic analysis were derived from two
716 whole dissociated hearts to collect cryosections and generate Visium datasets at 8.4 pcw (XY,
717 2 sections) and 9.7 pcw (XX, 4 sections). (**B**) Integrated UMAP representation of 49,227
718 profiled nuclei coloured by cell type. (**C**) UMAP representation of profiled nuclei as in (B) but
719 separated by sample. Arrows indicate cluster 12 (SMC) in each, but that all cell types are
720 present at each sample. (**D**) UMAP plots per sample indicating that all cell classes are also
721 represented in each sample. (**E**) Dot plot of top marker genes for each Class (y axis:
722 cardiomyocytes (I), endocardiovascular cells (II), stroma (III), epicardium (IV), blood (V) and
723 neural crest progeny (VI). The size of the dot represents the percent of nuclei with transcripts
724 at non-zero levels, and color intensity represents average log-normalized expression of the
725 gene where relative abundance of typical markers is indicative of cell class. (**F**) UMAP feature
726 plots of representative gene expression in Classes I to VI for *MYH7* (cardiomyocytes),
727 *PECAM1* (endothelial and endocardial cells), *EBF2* (stroma), *TBX18* (epicardium), *SPP1*
728 (immune cells) and *NRXN1* (neural crest). (**G**) Heatmap showing selected genes expressed
729 in the nine cardiomyocyte clusters of Class I compared with the minority populations of
730 lymphatic endothelium, Schwann cell precursors and neuroendocrine cells. Each column
731 displays gene expression of an individual cell and genes are listed in the rows.

732

Figure 2. Trajectory analysis of Classes I and III over time suggests a transient cardiomyofibroblast progenitor present at 4-6 pcw

(**A**) PHATE visualization of cardiomyocyte and stromal cells, colored by developmental stage, from cardiac single-cell RNA-seq data of seven human embryos at Carnegie stage (CS)12, CS13-14 and CS15-16 (Xu et al., 2023), one heart at 6.5-7 pcw (Asp et al., 2019), and this study's snRNAseq data from hearts at 8.6, 9.0 and 10.7 pcw. Boxed area in **A-D** delimits a cell population with greatest contribution from early stages. (**B**) Subset of PHATE plot from A, showing scRNA-seq data at 4-6 pcw, colored by original clusters from Xu et al., 2023. (**C**) Subset of PHATE plot from **A** showing snRNAseq data at 8.6, 9.0 and 10.7 pcw, colored by integrated clusters (cf. Fig. 1B). (**D**) Superimposition of Slingshot trajectory on PHATE plot in **A-C**, predicting cluster lineage bifurcations (black lines) from cluster 16, the "cardiomyofibroblast" (CmF; dashed square **A-D**). (**E**) Confusion matrix of percentages of cell types from our snRNAseq clusters (**C** on y axis) against new clusters after dataset integration (**D** on x axis). Fewer than 20% of the cells in cluster 16 (CmF) persist after 8.6 pcw. (**F**) Histogram showing percentages of cells/nuclei from each stage in each cluster from **D**, aligned with **E**'s x-axis. Fb2, SMC and CmVCnd cell types appear after 6.5 pcw, while CmA3, CmG2M and Fb3 were newly identified after 8.6 pcw. (**G**) Top panel shows four inheritance patterns (1-4) of the trajectory from cluster 16 (CmF) to 6 (CmMit) and 15 (Fb3). Bottom panel: DEGs of A>B defined as A > 0.5 and A/B > two-fold. 1: CmF and CmMit > Fb3 (inherited DEGs). 2: CmMit > CmF and Fb3 (non-inherited). CmF and Fb3 > CmMit (inherited DEGs). Fb3 > CmF and CmMit (non-inherited). Patterns 1 and 4 best fit the data, suggesting that CmF resembles a cardiomyocyte more than a fibroblast.

Figure 3. Spatial transcriptomics (ST) in 8.4 pcw and 9.7 pcw human heart sections show regionalized distributions of cardiac cell types

(**A**) Seurat UMAP plot of integrated spatial transcriptomic data from two 8.4 postconceptional week (pcw) and four 9.7 pcw heart sections. Each dot represents a tissue-covered spot from the Visium spatial capture slides. Fourteen clusters corresponding to cardiac cell types are listed. (**B**) Visualization of clustering on each heart section after ST data integration, with cluster annotations and colors matching the UMAP in A. (**C**) Spatial plots of gene expression, with highest in red and lowest in blue. RV, right ventricle; LV, left ventricle; RA, right atrium; LA, left atrium; Ao, aorta; SMC, (vascular) smooth muscle cells.

766 ## Figure 4. Corroboration of Class I marker expression

767 (First column: **A, E, I, M**) UMAPs showing gene expression of *MYL7*, *MYH6*, *MYH7* and
768 *BMP10* in cardiomyocyte Class I, indicating atrial and ventricular subclasses. (**B, C**) Spatial
769 transcriptomic (ST) plots of *MYL7* transcript distribution. (**D**) Immunofluorescence of MYL7,
770 with greater atrial than ventricular expression. (**F, G**) ST plots of *MYH6*. (**H**) MYH6 more
771 strongly immunostained atria than ventricles. (**J, K**) ST plot distribution of *MYH7*. (**L**)
772 Immunofluorescence of MYH7 in ventricular myocardium at 12.0 pcw. (**N, O**) ST plots of
773 *BMP10* . (**P**) *BMP10* transcripts detected by RNAscope in ventricular trabeculae and pectinate
774 muscles of the right atrium . (**B, F, G, J, K, N, O**) Highest expression in red and lowest in blue.
775 Ao, aorta; IVS, interventricular septum; LA, left atrium; LV, left ventricle; RA, right atrium; RV,
776 right ventricle. Scale bars: 250μm.

777

Figure 5: Deconvolution of heart ST data using snRNAseq reference reveals transcriptional heterogeneity in ST spots

(**A, C**) Deconvolution of spots of 8.4 pcw heart section A91 (**A**) and 9.7 pcw section A17 (**C**) using RCTD. The proportion of each cell type (cluster) from integrated snRNAseq data (Figure 1) is represented in pie charts for each spatial spot. Large pie charts represent the average proportion of each cell type in spatial clusters C0, C2, C3, C4, C10 and C13 from Figure 3B. (**B, D**) Cell-type proportions for CmVCnD, CmV1, CmG2M, CmA1, CmA4, CmA3, FbVIC, CmV2/subvalvular, EnTh, EndoCd, Fb1, Fb2, SMC, EpiCd and CmA2/node in spots of 8.4 pcw section A91 (**B**) and 9.7 pcw section A17 (**D**). Highest proportion is in red, lowest in blue. Note the consistency between snRNAseq cell types and their predicted spatial localization.

789 ## Figure 6: Spatial gene expression in outflow and atrioventricular valves

790 (**A-C, G-I**) Spatial plots of stromal class transcripts in representative sections of 8.4 pcw heart,
791 with highest expression in red and lowest in blue. (**C, I**) Co-expression plots of *PENK* (red)
792 and *ACTA1* or *MEOX1* (green), with highest expression of each in the most saturated color
793 and equal co-expression in yellow. (**C', I'**) Enlargement of the atrioventricular cushion region
794 shown in panels **C** and **I**. (**D, E**) RNAscope *in situ* hybridization of *PENK* and *ACTA1* in a 9.0
795 pcw heart section. (**F, F'**) Double-staining showing expression of *PENK* (red) and *ACTA1*
796 (green) mRNAs in the same section. *PENK* is expressed in atrioventricular valve leaflets, while
797 *ACTA1* labels chordae tendineae. (**F'**) Enlargement of the area marked by a dotted square in
798 the adjacent section from panel F. (**J**) *PRRX1* in the aortic valve of a 7.0 pcw heart. (**K, L**)
799 Spatial expression of *MEOX1* and *PRRX1* detected by RNAscope in a 9.0 pcw heart. (**M, M'**)
800 Double-staining of *PENK* (red) and *MEOX1* (green) mRNAs in the same section. (**M'**)
801 Enlargement of the area marked by a dotted square in the adjacent section from panel M.
802 *PENK* is expressed in the inferior atrioventricular endocardial cushion, partly overlapping
803 (arrows in **I'**) with *MEOX1*. Ao, aorta; CT, chordae tendineae; iavc, inferior atrioventricular
804 endocardial cushion (Anderson et al., 2003); LA, left atrium; LCA, left coronary artery; LV, left
805 ventricle; MV, mitral valve; RA, right atrium; RCA, right coronary artery; RV, right ventricle; TV,
806 tricuspid valve; sb, subvalvular domain (septal bridge); *, blood clots. Arrows (**J),** coronary
807 arteries. Scale bars: 250 μm except D, 500 μm.

808

809 ## Figure 7: Parasympathetic ganglia and nerve markers

810 (**A, B**) Spatial plots of transcripts enriched in conduction and nervous system on an 8.4 pcw
811 heart section, with highest expression in red and lowest in blue. (**C**) Co-expression plots of
812 *ISL1* (red) and *PRRX1* (green), with highest expression of each in the most saturated color
813 and equal co-expression in yellow. **(A', B'**) RNAscope *in situ* hybridization detected *ISL1* and
814 *PRRX1* in the same sections. (**C'**) Complementary expression of *ISL1* (green) and *PRRX1*
815 (red) in a parasympathetic ganglion. (D-F) *ISL1*, *PRRX1* and *ACTA1* respective RNAscope
816 probes co-hybridized in another section from same 7 pcw heart. At atrioventricular septum
817 intersection in box, enlarged in D'-F', localized expression of each transcript is indicated with
818 arrows. Ao, aorta; b, blood; ivs, interventricular septum; LA, left atrium; LV, left ventricle; RA,
819 right atrium; RV, right ventricle. Scale bars (**A-C**): 250μm; (**D-F**): 200 μm.

820

821 Figure 8. Three-dimensional reconstruction of vascular and nerve
822 scaffolds over time

823 (**A**) UMAP visualization of *PRPH* by snRNAseq. (**B**) Spatial plots showing *PRPH* expression
824 in cardiac ganglion (g) on an 8.4 pcw heart section. (**C**) Immunofluorescence detection of
825 PRPH in a 9.0 pcw heart section. PRPH is expressed in the nerves (arrows) and ganglia (g).
826 (**D**) UMAP visualization of *PECAM1* by snRNAseq. (**E**) Spatial plots showing *PECAM1*
827 transcripts in an 8.4 pcw heart section, with highest expression in red and lowest expression
828 in blue. (**F**) PECAM1 (CD31) immunofluorescence in vascular endothelial cells (arrows) in a
829 9.0 pcw heart section. (**G-L**) Whole-mount immunofluorescence of both PECAM-1 (CD31, red
830 [**G**] or magenta [**J**]) and PRPH (yellow) in 9.0 and 10.0 pcw hearts. (**G, L**) 3D reconstructions
831 from light-sheet fluorescent microscopy (LSFM) image stacks show parallel networks of
832 vessels (PECAM1+) and nerves (PRPH+) in 9.1 and 10.1 pcw hearts. (**H, K**) Top views of
833 hearts in **G** and **J**. (**I, L**) LSFM reconstructions of the pulmonary valve showing that valve
834 leaflets, unlike the great vessels, are not innervated. (**B, E**) Highest expression in red, lowest
835 in blue. Ao, aorta; AoV, aortic valve; LCA, left coronary artery; LV, left ventricle; Pt, pulmonary
836 trunk; RCA, right coronary artery; RV, right ventricle. Scale bars: (**G, J**) 500 μm; (**H**) 400 μm;
837 (**I**) 300 μm; (**K**, **L**) 150 μm.

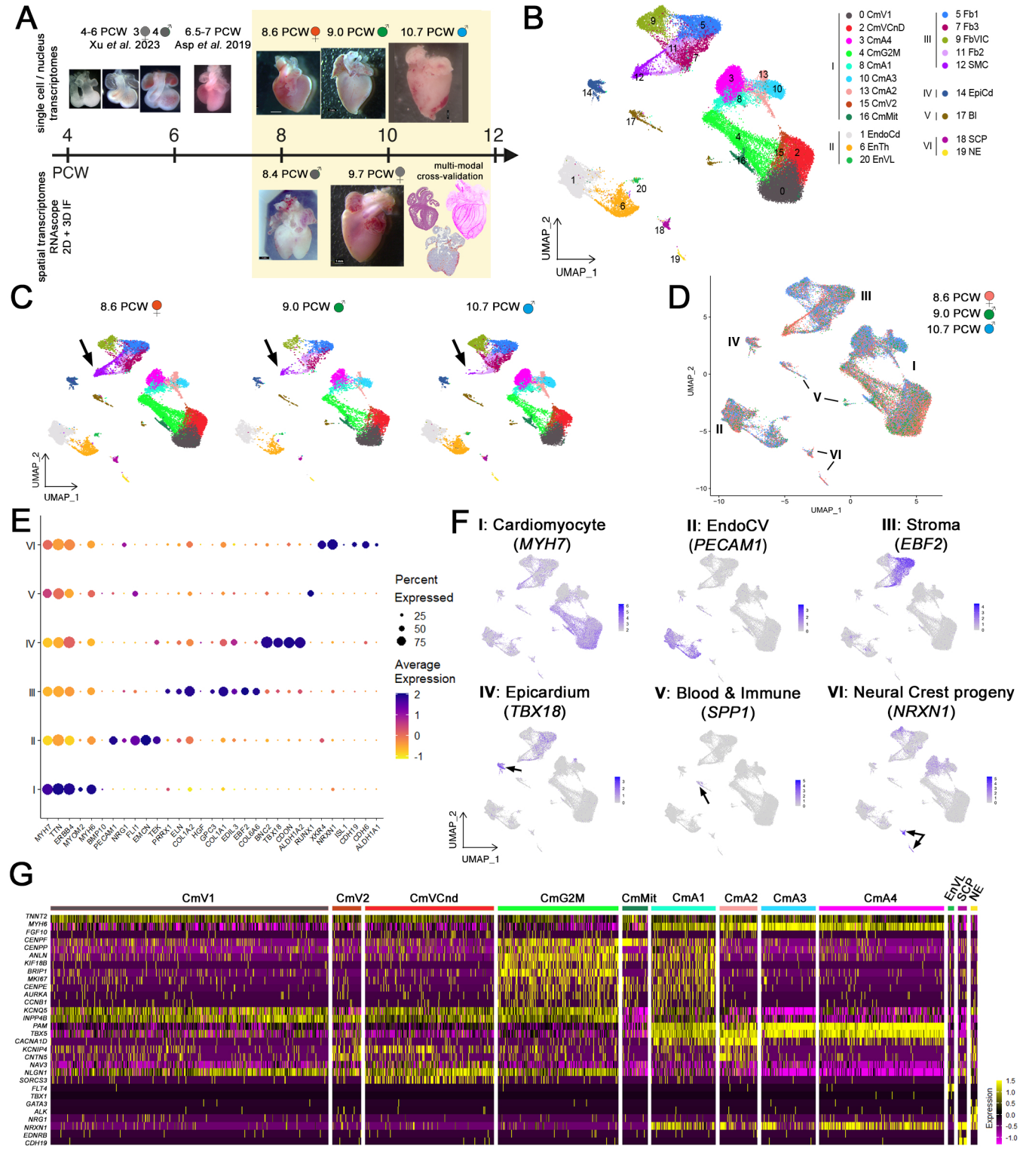
A
4-6 PCW
Xu et al. 2023
6.5-7 PCW
Asp et al. 2019
8.6 PCW
9.0 PCW
10.7 PCW
single cell / nucleus transcriptomes
4
6
8
10
12
PCW
8.4 PCW
9.7 PCW
multi-modal cross-validation
spatial transcriptomes
RNAscope
2D + 3D IF
B
0 CmV1
2 CmVCnD
3 CmA4
4 CmG2M
8 CmA1
10 CmA3
13 CmA2
15 CmV2
16 CmMit
1 EndoCd
6 EnTh
20 EnVL
5 Fb1
7 Fb3
9 FbVIC
11 Fb2
12 SMC
14 EpiCd
17 Bl
18 SCP
19 NE
UMAP_2
UMAP_1
C
8.6 PCW
9.0 PCW
10.7 PCW
D
8.6 PCW
9.0 PCW
10.7 PCW
E
Percent Expressed
25
50
75
Average Expression
2
1
0
-1
MYH7
TTN
ERBB4
MYOM2
MYH6
BMP10
PECAM1
NRG1
FLI1
EMCN
TBX1
PRRX1
ELN
COL1A2
HGF
GPC3
COL1A1
EDIL3
EBF2
COL6A6
BNC2
TBX18
CDON
ALDH1A2
RUNX1
XKR4
NRXN1
ISL1
CDH19
CDH6
ALDH1A1
F
I: Cardiomyocyte (MYH7)
II: EndoCV (PECAM1)
III: Stroma (EBF2)
IV: Epicardium (TBX18)
V: Blood & Immune (SPP1)
VI: Neural Crest progeny (NRXN1)
G
CmV1
CmV2
CmVCnd
CmG2M
CmMit
CmA1
CmA2
CmA3
CmA4
EnVL
SCP
NE
TNNT2
MYH6
FGF10
CENPF
CENPP
ANLN
KIF18B
BRIP1
MKI67
CENPE
AURKA
CCNB1
KCNQ5
INPP4B
PAM
TBX5
CACNA1D
KCNIP4
CNTN5
NAV3
NLGN1
SORCS3
FLT4
TBX1
GATA3
ALK
NRG1
NRXN1
EDNRB
CDH19
Expression

Figure 1

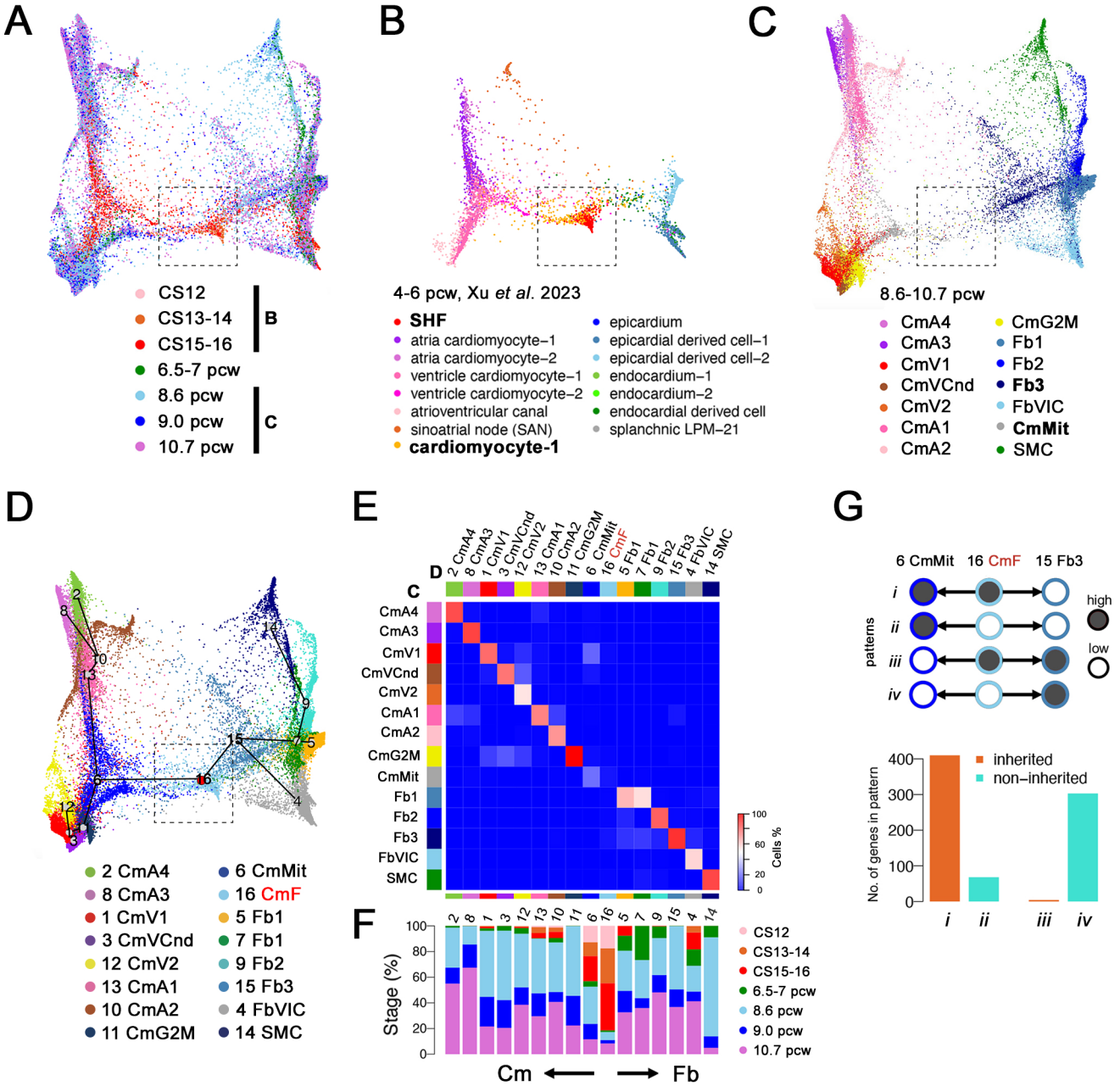
A
CS12
CS13-14
CS15-16
B
6.5-7 pcw
8.6 pcw
9.0 pcw
10.7 pcw
C
B
4-6 pcw, Xu et al. 2023
SHF
atria cardiomyocyte−1
atria cardiomyocyte−2
ventricle cardiomyocyte−1
ventricle cardiomyocyte−2
atrioventricular canal
sinoatrial node (SAN)
cardiomyocyte-1
epicardium
epicardial derived cell−1
epicardial derived cell−2
endocardium−1
endocardium−2
endocardial derived cell
splanchnic LPM−21
C
8.6-10.7 pcw
CmA4
CmA3
CmV1
CmVCnd
CmV2
CmA1
CmA2
CmG2M
Fb1
Fb2
Fb3
FbVIC
CmMit
SMC
D
2 CmA4
8 CmA3
1 CmV1
3 CmVCnd
12 CmV2
13 CmA1
10 CmA2
11 CmG2M
6 CmMit
16 CmF
5 Fb1
7 Fb1
9 Fb2
15 Fb3
4 FbVIC
14 SMC
E
Cells %
F
Stage (%)
CS12
CS13-14
CS15-16
6.5-7 pcw
8.6 pcw
9.0 pcw
10.7 pcw
Cm
Fb
G
6 CmMit
16 CmF
15 Fb3
patterns
high
low
No. of genes in pattern
inherited
non−inherited

Figure 2

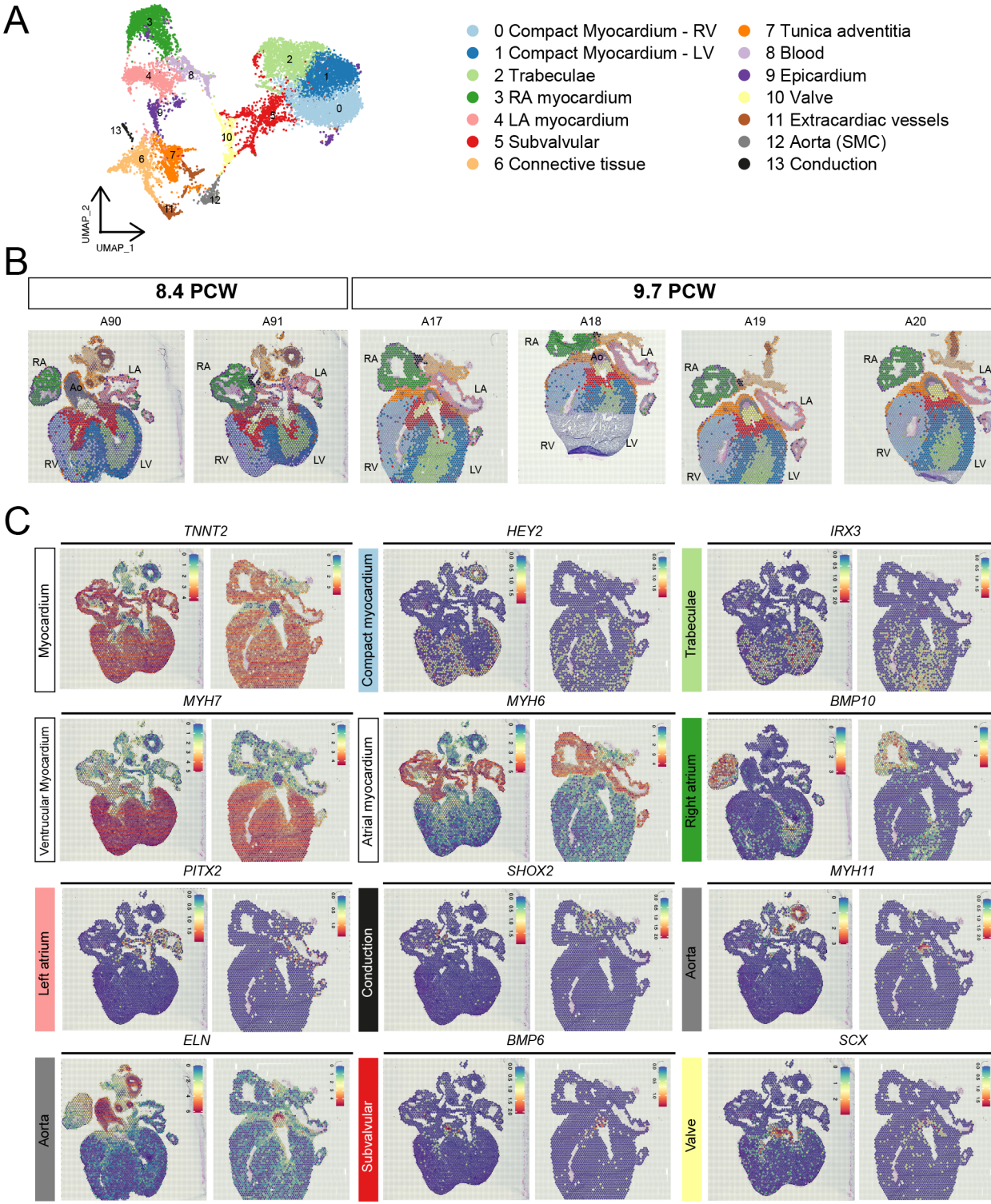
A
0 Compact Myocardium - RV
1 Compact Myocardium - LV
2 Trabeculae
3 RA myocardium
4 LA myocardium
5 Subvalvular
6 Connective tissue
7 Tunica adventitia
8 Blood
9 Epicardium
10 Valve
11 Extracardiac vessels
12 Aorta (SMC)
13 Conduction
UMAP_1
UMAP_2
B
8.4 PCW
9.7 PCW
A90
A91
A17
A18
A19
A20
RA
LA
Ao
RV
LV
C
TNNT2
HEY2
IRX3
Myocardium
Compact myocardium
Trabeculae
MYH7
MYH6
BMP10
Ventrucular Myocardium
Atrial myocardium
Right atrium
PITX2
SHOX2
MYH11
Left atrium
Conduction
Aorta
ELN
BMP6
SCX
Aorta
Subvalvular
Valve

Figure 3

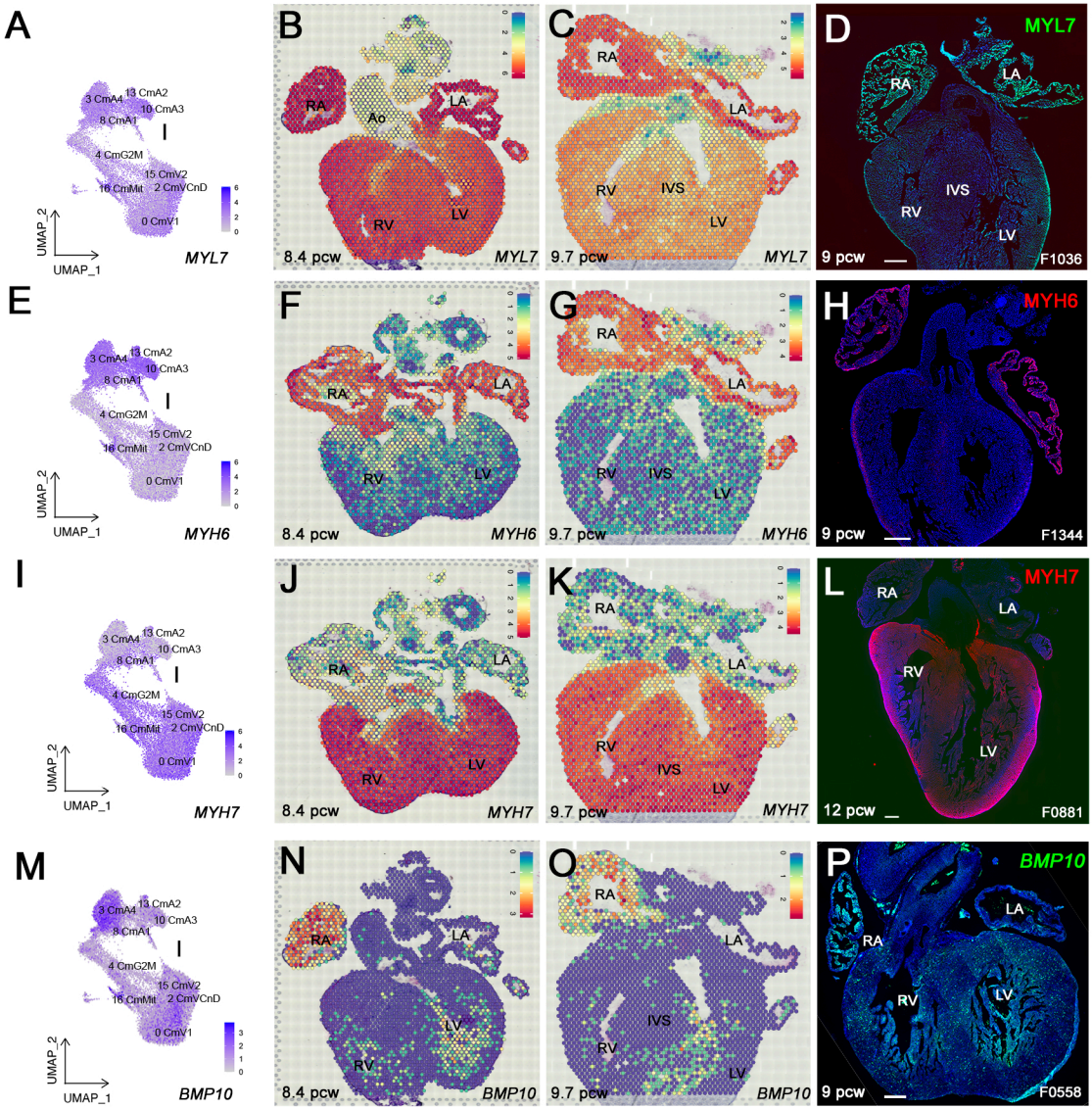
A
B
C
D
MYL7
E
F
G
H
MYH6
I
J
K
L
MYH7
M
N
O
P
BMP10
UMAP_1
UMAP_2
3 CmA4
13 CmA2
10 CmA3
8 CmA1
4 CmG2M
15 CmV2
16 CmMit
2 CmVCnD
0 CmV1
RA
LA
Ao
RV
LV
IVS
8.4 pcw
9.7 pcw
9 pcw
12 pcw
F1036
F1344
F0881
F0558

Figure 4

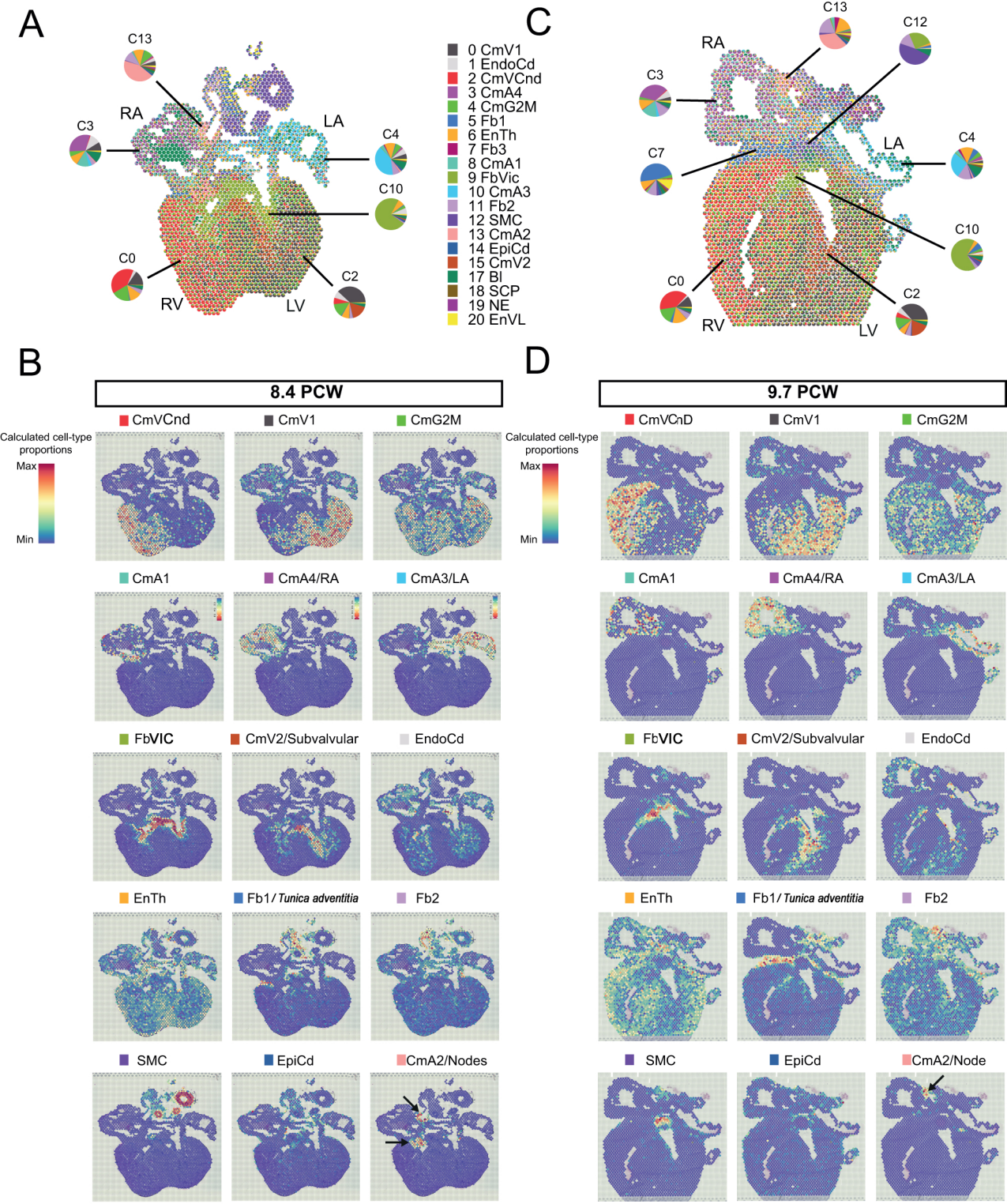
A
C13
RA
C3
LA
C4
C10
C0
RV
LV
C2
0 CmV1
1 EndoCd
2 CmVCnd
3 CmA4
4 CmG2M
5 Fb1
6 EnTh
7 Fb3
8 CmA1
9 FbVic
10 CmA3
11 Fb2
12 SMC
13 CmA2
14 EpiCd
15 CmV2
17 Bl
18 SCP
19 NE
20 EnVL
C
C13
C12
RA
C3
C7
LA
C4
C10
C0
RV
LV
C2
B
8.4 PCW
Calculated cell-type proportions
Max
Min
CmVCnd
CmV1
CmG2M
CmA1
CmA4/RA
CmA3/LA
FbVIC
CmV2/Subvalvular
EndoCd
EnTh
Fb1/ Tunica adventitia
Fb2
SMC
EpiCd
CmA2/Nodes
D
9.7 PCW
Calculated cell-type proportions
Max
Min
CmVCnD
CmV1
CmG2M
CmA1
CmA4/RA
CmA3/LA
FbVIC
CmV2/Subvalvular
EndoCd
EnTh
Fb1/ Tunica adventitia
Fb2
SMC
EpiCd
CmA2/Node

Figure 5

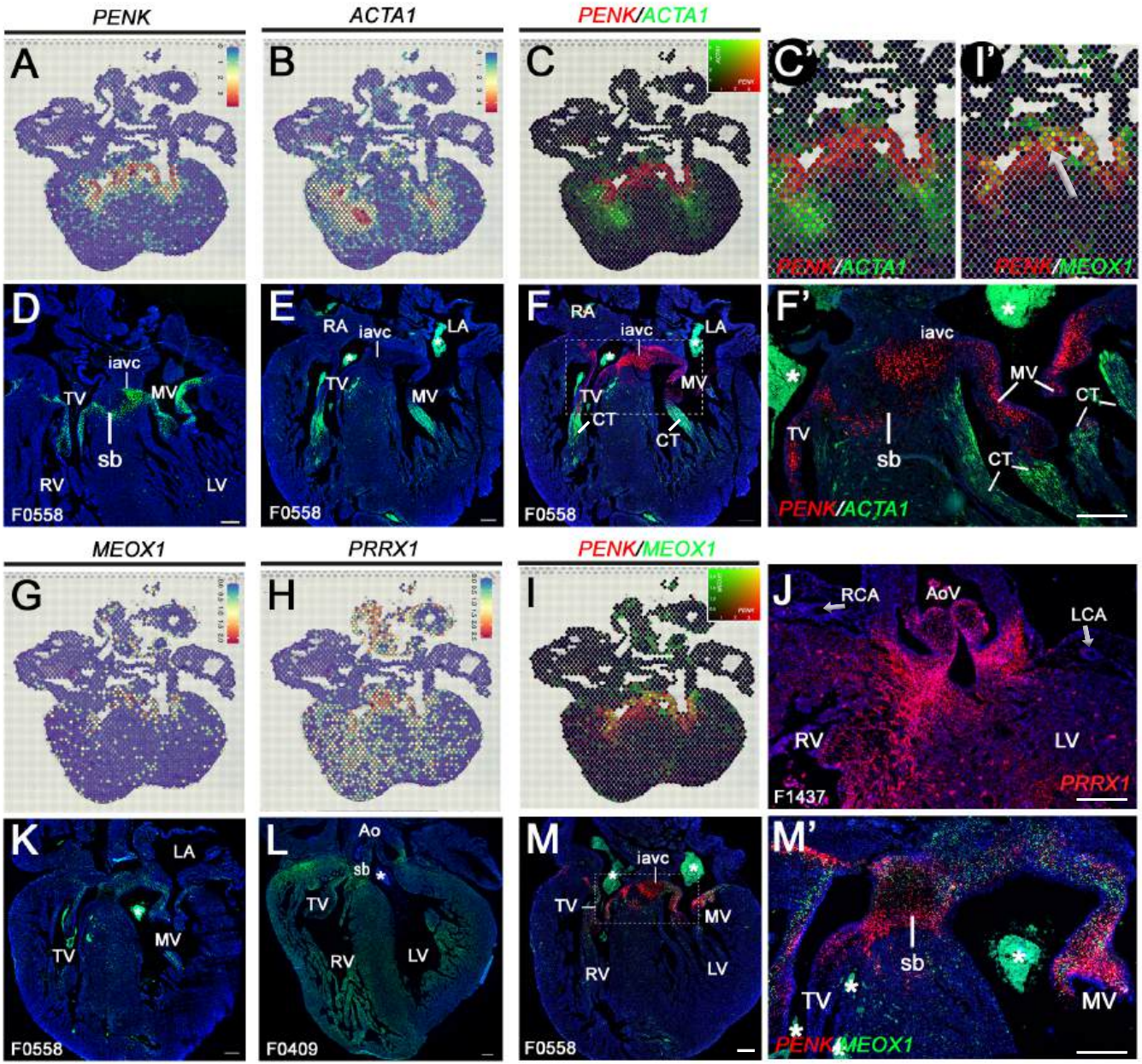
PENK
ACTA1
PENK/ACTA1
A
B
C
C'
I'
PENK/ACTA1
PENK/MEOX1
D
E
F
F'
iavc
TV
MV
sb
RV
LV
F0558
RA
LA
CT
MEOX1
PRRX1
PENK/MEOX1
G
H
I
J
RCA
AoV
LCA
F1437
PRRX1
K
L
M
M'
Ao
F0409
PENK/MEOX1

Figure 6

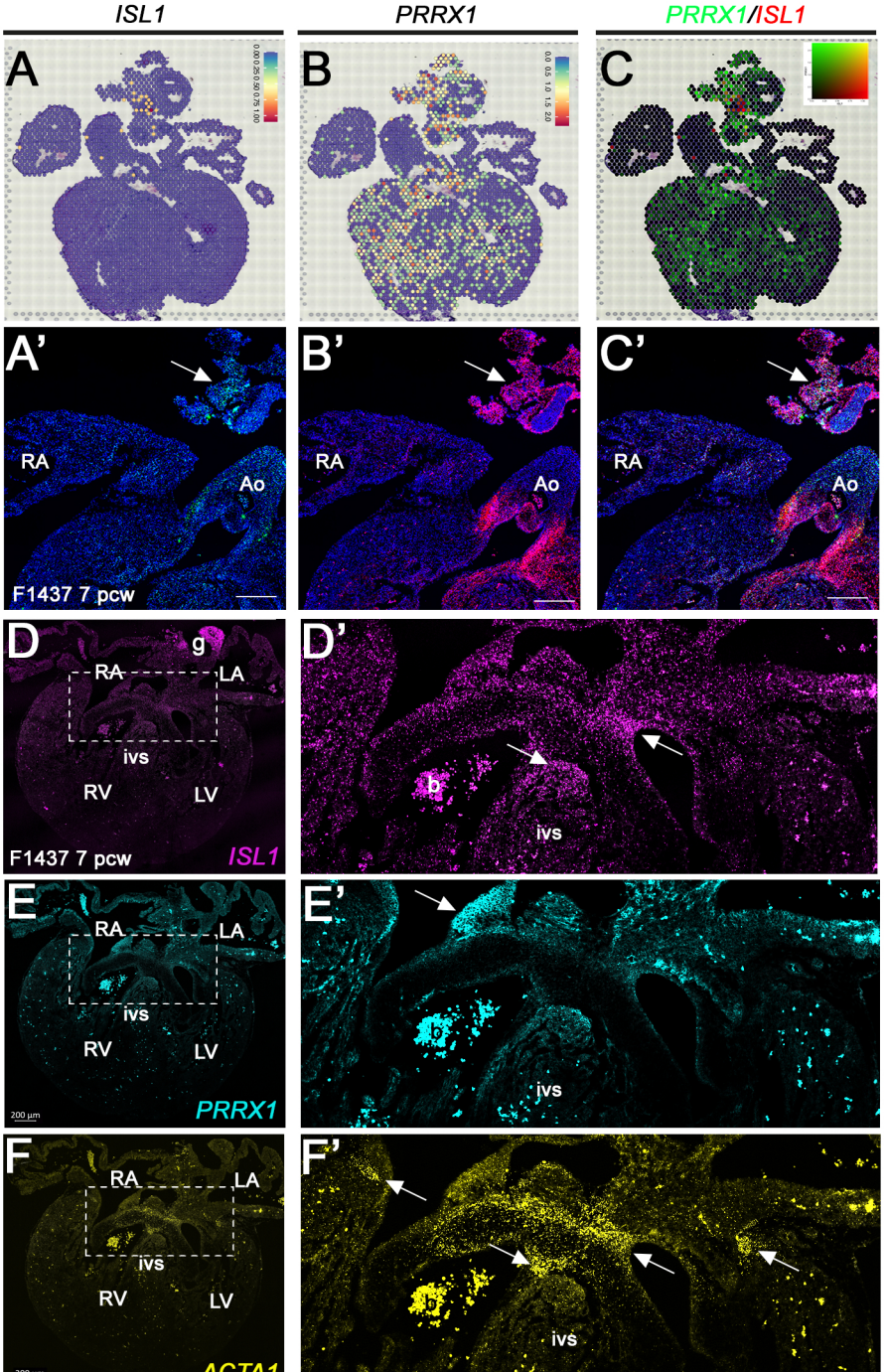
ISL1
PRRX1
PRRX1/ISL1
A
B
C
A'
B'
C'
RA
Ao
F1437 7 pcw
D
D'
g
RA
LA
ivs
RV
LV
b
F1437 7 pcw
ISL1
E
E'
PRRX1
200 µm
F
F'
ACTA1
200 µm

Figure 7

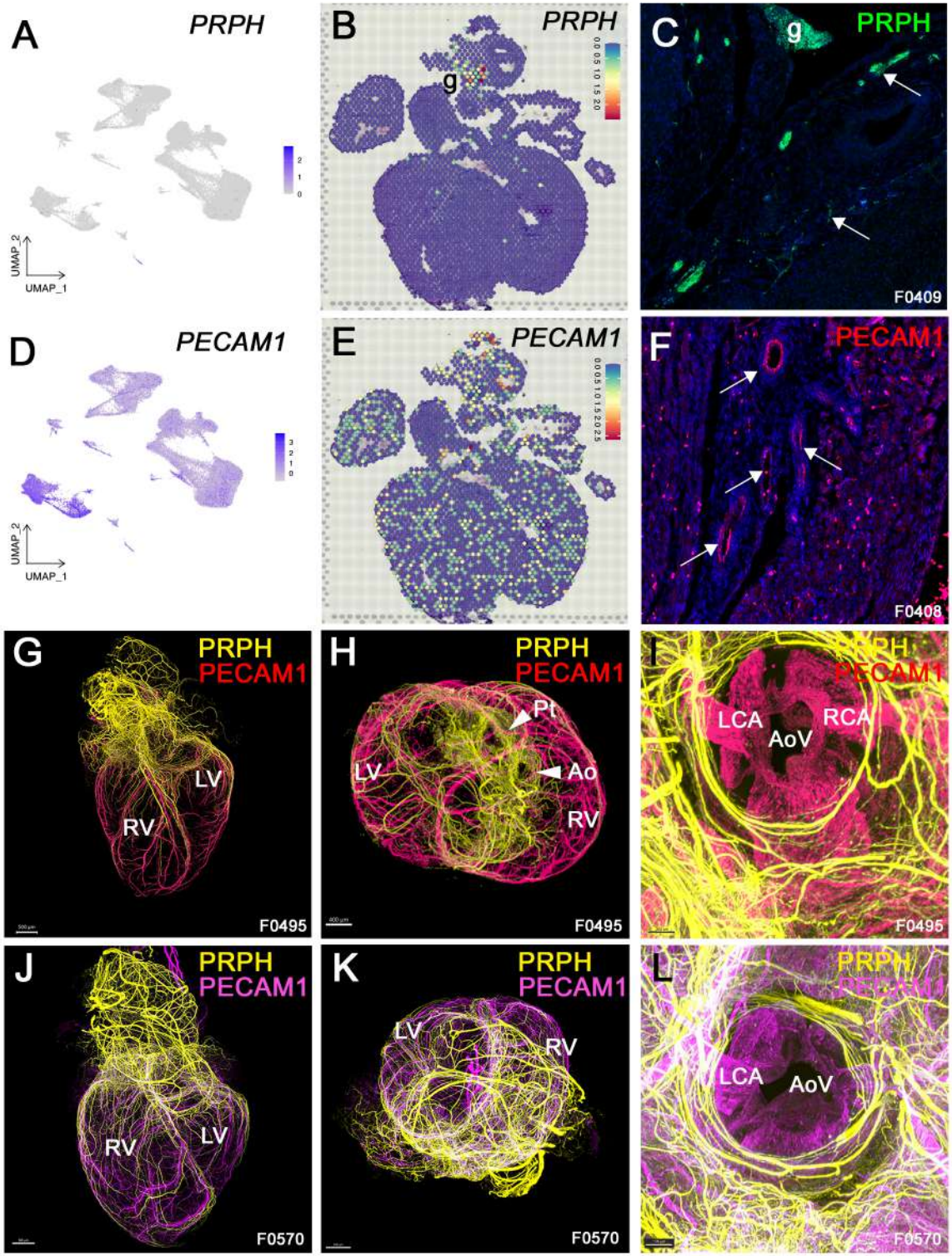
A
PRPH
UMAP_2
UMAP_1
B
PRPH
g
C
g
PRPH
F0409
D
PECAM1
UMAP_2
UMAP_1
E
PECAM1
F
PECAM1
F0408
G
PRPH
PECAM1
LV
RV
F0495
H
PRPH
PECAM1
Pt
LV
Ao
RV
F0495
I
PRPH
PECAM1
LCA
AoV
RCA
F0495
J
PRPH
PECAM1
RV
LV
F0570
K
PRPH
PECAM1
LV
RV
F0570
L
PRPH
PECAM1
LCA
AoV
F0570

Figure 8